Atmospheric
Chemistry
and Physics
Discussions

Open Access

EGU

1 **Chemical composition and source apportionment of atmospheric aerosols on**

2 **the Namibian coast**

3 **Danitza Klopper[1], Paola Formenti[2], Andreas Namwoonde[3], Mathieu Cazaunau[2], Servanne**

4 **Chevaillier[2], Anaïs Feron[2], Cécile Gaimoz[2], Patrick Hease[2], Fadi Lahmidi[2], Cécile Mirande-Bret[2],**

5 **Sylvain Triquet[2], Zirui Zeng[2] and Stuart J. Piketh[1]**

6

7 [1] North-West University, School for Geo- and Spatial Sciences, Potchefstroom, South Africa

8 [2] Laboratoire Interuniversitaire des Systèmes Atmosphériques (LISA), UMR CNRS 7583, Université Paris-

9 Est-Créteil, Université de Paris, Institut Pierre Simon Laplace, Créteil, France

10 [3] SANUMARC, University of Namibia, Henties Bay, Namibia

11

12 **Corresponding author:** paola.formenti@lisa.u-pec.fr

13

14 **Abstract**

15 The chemical composition of aerosols is of particular importance to assess their interactions with radiation,

16 clouds and trace gases in the atmosphere, and consequently their effects on air quality and the regional

17 climate. In this study, we present the results of the first long-term dataset of the aerosol chemical

18 composition at an observatory on the coast of Namibia, facing the southeast Atlantic Ocean. Aerosol samples

19 in the mass fraction of particles smaller than 10 μm in aerodynamic diameter (PM_{10}) were collected during

20 26 weeks between 2016 and 2017 at the ground-based Henties Bay Aerosol Observatory (HBAO; 22°6'S,

21 14°30'E, 30 m above mean sea level). The resulting 385 filter samples were analysed by X-ray fluorescence

22 and ion-chromatography for 24 inorganic elements and 15 water-soluble ions.

23 Statistical analysis by positive matrix factorization and back-trajectory modelling identified five major

24 sources, sea salt (mass concentration: 70.8 ± 0.2%), marine biogenic (13.5 ± 0.8%), mineral dust (9.9 ±

25 0.1%), secondary products (3.2 ± 1.0%) and heavy metals (2.3 ± 2.5%). While the contribution of sea salt

26 aerosol was persistent, as the dominant wind direction was south-westerly and westerly from the open

27 ocean, the occurrence of mineral dust was episodic and coincided with high wind speeds from the south-

28 southeast and the north-northwest, along the coastline. Concentrations of heavy metals measured at HBAO

29 were higher than reported in the literature from measurements over the open ocean. The heavy metals (V,

30 Cr, Nd and Mn) measured at the site were attributed to mining activities and the combustion of heavy fuels

31 in commercial ship traffic across the Cape of Good Hope sea route. Fluoride concentrations up to 25 μg m^{-3}

32   were measured, as in heavily polluted areas in China. This is surprising and a worrisome result that has

33   profound health implications and deserves further investigation. Although no clear signature for biomass

34   burning could be determined, the source of secondary products identified by PMF was described by a

35   mixture of aerosols typically emitted by biomass burning, but also by other biogenic activities. Episodic

36   contributions with moderate correlations between NO_3^-, nss-SO_4^{2-} (higher than 2 µg m^{-3}) and nss-K^+, were

37   observed, further indicative of the potential for an episodic source of biomass burning.

38   Sea salt accounted for up to 57% of the measured mass concentrations of SO_4^{2-} and the non-sea salt fraction

39   contributed mainly to the secondary product and marine biogenic sources identified by PMF. The marine

40   biogenic contribution is attributed to efficient oxidation in the moist marine atmosphere of sulphur-

41   containing gas-phase emitted by marine phytoplankton in the fertile waters offshore in the Benguela

42   Upwelling System.

43   The data presented in this paper provide first-ever information on the temporal variability of aerosol

44   concentrations in the Namibian marine boundary layer and the links to meteorological conditions shaping

45   the transport patterns of aerosols from different sources. This data can be used to provide context for

46   intensive observations in the area.

47   **Keywords:** aerosols, chemical composition, transport, Namibia, positive matrix factorisation

1. Introduction

49   Atmospheric aerosol particles are emitted from both natural and anthropogenic sources. Depending on

50   their chemical and physical characteristics, airborne aerosol particles modify the Earth's radiative budget

51   by scattering and absorbing solar and terrestrial radiation and by altering cloud lifetime and microphysical-

52   and optical properties (Seinfeld and Pandis, 2006). The variability in their source distribution and short

53   lifetime in the atmosphere (typically less than 10 days for particles below 1 µm in diameter, and shorter for

54   larger particles) results in an uneven horizontal and vertical spatial distribution of concentrations and

55   physicochemical properties (Seinfeld and Pandis, 2006). As a consequence, their effects on regional

56   atmospheric dynamics and processes are unevenly spread and constantly changing, in stark contrast to the

57   long-lived greenhouse gases which are well-distributed around the globe (Boucher, 2013).

58   The Namibian coast, and more generally the southeast Atlantic region of southern Africa, is amongst the

59   global areas of interest to study aerosols and their role on Earth's climate (De Graaf et al., 2014; Muhlbauer

60   et al., 2014; Painemal et al., 2014a, 2014b, 2014c; Wilcox, 2010; Zuidema et al., 2009). Local meteorological

61   conditions in this coastal desert environment are sustained by the effect of cold ocean currents in the

62   Benguela Upwelling System (BUS), one of the strongest oceanic upwelling systems in the world, with very

63   low sea surface temperatures all year round, reaching a minimum in the austral winter (Cole and

64   Villacastin, 2000; Nelson and Hutchings, 1983). This has a stabilising effect on the lower troposphere,

65   resulting in the formation of a semi-permanent stratocumulus (Sc) cloud deck extending between 10–30°S,

66   10°W–10°E, that tops the marine boundary layer at ~850 hPa (Muhlbauer et al., 2014; Wood, 2015) and is

67   of global significance for Earth's radiation budget (Klein and Hartmann, 1993; Johnson et al., 2004;

68   Muhlbauer et al, 2014; Wood, 2015).

69   The region is also known for its high marine phyto- and zoo-plankton specifically in the northern BUS

70   (Louw et al., 2016). The marine biogenic activity results in the release of gaseous compounds containing

71   sulphur (dimethylsulphide (DMS), SO_2, H_2S…) to the atmosphere (Andreae et al., 1994), whose oxidation,

72   particularly in this marine environment, could produce new aerosol particles contributing to the cloud

73   droplet number concentration of the Sc clouds (Charlson et al., 1987; Andreae et al., 1995). The region is

74   also known for the seasonal transport above the Sc of optically-thick and wide-spread smoke layers of

75   biomass burning aerosols emitted from forest fires in southern Africa in the austral dry season (August to

76   October; Lindesay et al., 1996; Swap et al., 2003).

77   Despite their relevance, very limited research has been conducted to assess the seasonal cycle and long-

78   term variability of the aerosol mass concentration and chemical composition in the region (Andreae et al.,

79   1995; Annegarn et al., 1983; Dansie et al., 2017; Eltayeb et al., 1993; Formenti et al., 1999, 2003b; 2018;

80   Zorn et al., 2008). To fill this gap, the long-term surface monitoring Henties Bay Aerosol Observatory

81   (HBAO) was established in 2012 on the campus of the University of Namibia's Sam Nujoma Marine and

82   Coastal Resources Research Centre (SANUMARC), along the Namibian coast (22°S; 14°E). HBAO faces the

83   open ocean in an arid environment, far from major point sources of pollution. Episodically through the year,

84   and seasonally between April to end of July, the station is affected by polluted air masses containing light-

85   absorbing aerosols, mostly from vegetation burning (Formenti et al., 2018).

86   In this paper, we present the results of the very first long-term measurements of aerosol elemental and

87   water-soluble ionic composition from the analysis of filter samples in the mass fraction of particles smaller

88   than 10 μm in aerodynamic diameter (PM_{10} fraction) that were collected during 26 non-consecutive

89   sampling weeks in 2016 and 2017. The paper looks into the temporal variability of measured elemental

90   and water-soluble ionic concentrations and yields the first source apportionment to the PM_{10} loading,

91   which is linked to the synoptic pathways of air mass transport.

92   The research presented in this study is relevant to the recent intensive observational efforts that took place

93   in Namibia in 2016 and 2017 (Zuidema et al., 2016). Specifically, it provides the long-term context to the

94   intensive filter sampling that was conducted in Henties Bay as part of the Aerosols, RadiatiOn and CLOuds

95   in southern Africa (AEROCLO-sA) project (Formenti et al., 2019).

96   **2. Experimental methods**

97   The HBAO station of Henties Bay, Namibia (22.09°S, 14.26°E; 30 m above mean sea level (amsl)

98   http://www.hbao.cnrs.fr/, last access: 22 May 2019) is situated 100 m from the shoreline and is

99   surrounded by an arid environment with little to no vegetation, as shown in Figure 1. Henties Bay is located

100   approximatively 100 km north of Walvis Bay, the largest commercial harbour of Namibia (Namport, 2018).

101   Formenti et al. (2018) showed that the location can be considered as baseline for a large part of the year

102   (August to late April). However, from May to end of July it is impacted by the synoptic transport of light-

103   absorbing aerosols mostly from vegetation burning in southern Africa and possibly but episodically by

104   anthropogenic sources, such as heavy-fuel combustion by commercial ships travelling along the coast,

105   especially along the Cape of Good Hope sea route (eg. Chance et al., 2015; Tournadre, 2014; Zhang et al.,

106   2010).

107   **2.1   Aerosol filter sampling and analysis**

108   An automated sequential air sampler (model Partisol Plus 2025i, Thermo Fisher Scientific, Waltham, MA

109   USA) was used to collect aerosol particles on 47-mm Whatman Nucleopore polycarbonate filters (1-µm

110   pore size). Air was sampled at a flow rate of 1 m^3 h^{-1} through a certified inlet (Rupprecht and Patashnick,

111   Albany, New York, USA) located on the rooftop terrace above the instrument, and collecting aerosols

112   particles of aerodynamic diameter lower than 10 µm (PM_{10} fraction).

113   Individual filter samples were collected for 9 hours during the day (from 9 h to 18 h UTC) and during the

114   night (from 21 h to 6 h UTC) on an intermittent week on/week off schedule. One blank sample per time

115   series was collected. The whole dataset consisted of 385 samples.

116   Elemental concentrations of 24 elements (Na, Mg, Al, Si, P, S, Cl, K, Ca, Ti, V, Cr, Mn, Fe, Co, Ni, Cu, Zn, As, Sr,

117   Pb, Nd, Cd, Ba) were obtained at LISA by wavelength-dispersive X-ray fluorescence (WD-XRF) using a PW-

118   2404 spectrometer (Panalytical, Almelo, Netherlands), according to the protocol previously described by

119   Denjean et al. (2016). The relative analytical uncertainty on the measured atmospheric concentrations

120   (expressed in ng m^{-3}) is 5%, equal to the percent error on the certified mono- and bi-elemental standard

121   concentrations (Micromatter Inc., Surrey, Canada) used for calibration of the XRF apparatus.

122   Concentrations of elements from Na to Ca were corrected for the self-attenuation effects in large particles

123   as proposed by Formenti et al. (2010).

124   The concentrations of 16 water-soluble ions (F^-, propionate, formate, acetate, methanesulfonic acid (MSA),

125   Cl^-, Br^-, NO_3^-, PO_4^{3-}, SO_4^{2-}, oxalate, Na^+, NH_4^+, K^+, Ca^{2+} and Mg^{2+}) were obtained at LISA by ion chromatography

126   (IC) with a Metrohm IC 850 device (injection loop of 100 µl). For anionic species, the IC was equipped with

127   MetrosepA supp 7 (250/4.0mm) column associated with a MetrosepA supp 7 guard pre-column heated at

128 45°C. For simultaneous separation of inorganic and short-chain organic anions, elution has been realised

129 with the following elution gradient (eluent weak:Na_2CO_3/$NaHCO_3$ (0.28/0.1mM) and eluent strong:

130 Na_2CO_3/$NaHCO_3$ (28/10mM): 100% eluent weak from 0 to 23.5 minutes; then 15% eluant strong from 23.5

131 to 52 minutes and 100% eluent weak to finish. The elution flow rate was 0.8 ml min^{-1}. For cationic species,

132 IC has been equipped with a Metrosep C4 (250/4.0mm) column associated to a Metrosep C4 guard column

133 heated at 30°C. Elution has been realised with an eluant composed with 0.7 mM of dipicolinic acid and

134 1.7mM of nitric acid. The elution flow rate was 0.9 ml min^{-1}. The uncertainty of water-soluble ionic

135 concentrations (also expressed in ng m^{-3}) is within 5%, the maximum uncertainty obtained during

136 calibration by standard certified mono- and multi-ionic solutions.

137 For each chemical species, the minimum quantification limit (MQL) was calculated as 10 times the square

138 root of the standard deviation of the concentration of laboratory blank samples, corresponding to filter

139 membranes prepared as actual samples but stored and analysed without exposure to external air. Only

140 values above MQL are included in further analyses.

141 A quality-check assessment of the analysis was performed by comparing the concentrations of Cl, Mg, K, Ca,

142 Na and SO_4^{2-}/S measured by IC and XRF (Figure S1). The comparison revealed a good linear correlation

143 between the two datasets, with the coefficient of determination (R^2) exceeding 0.85 for all the elements.

144 However, some differences in the slopes of the linear correlations are observed when comparing the 2016

145 and 2017 datasets for Cl$^-$/Cl, Na$^+$/Na, and Mg^{2+}/Mg. Slopes were 1.3 ± 0.1 (2016) and 1.0 ± 0.1 (2017), 1.3

146 ± 0.1 (2016) and 0.9 ± 0.1 (2017), and 1.3 ± 0.1 (2016) and 1.5 ± 0.2 (2017) for Cl$^-$/Cl, Na$^+$/Na, and Mg^{2+}/Mg,

147 respectively. Conversely, no annual dependence was observed in the slopes of the linear correlations for

148 Ca^{2+}/Ca (0.8 ± 0.1), K$^+$/K (0.8 ± 0.1) and SO_4^{2-}/S (2.7 ± 0.3). These values are in general terms consistent

149 with expectations that these elements, mostly but not exclusively composing sea salt, should be

150 predominantly soluble in water. However, ratios higher than unity are obtained for Cl$^-$/Cl and Na$^+$/Na for

151 2016, and Mg^{2+}/Mg for both years. Although no specific sampling nor analytical problems were found, the

152 further comparison of their proportions to those expected for seawater (Seinfeld and Pandis, 2006)

153 suggested to discard the XRF results and only use the values obtained by IC for those three elements. For

154 Ca^{2+}/Ca, K$^+$/K and SO_4^{2-}/S, ratios are consistent with previous observations in marine environments

155 impacted by mineral dust (Formenti et al., 2003a).

156 **2.2   Local winds, air mass trajectories and synoptic meteorology**

157 Local wind speed and direction were measured with two anemometers also located on the rooftop of HBAO,

158 first, a Campbell Scientific 05103, replaced with a Vaisala WXT530 from September 2017 onwards.

159 Measurements were stored as 5-minute averages. Wind data was available for all of 2016 and 55% of the

160 aerosol sampling periods in 2017 (no wind data were available during 19 – 26 May and 7 – 14 July 2017).

161 The NOAA Hybrid Single-Particle Lagrangian Integrated Trajectory (HYSPLIT) model (Stein et al., 2015)
162 was used to evaluate the origin and transport pathway of air masses to HBAO. Seventy-two-hour back-
163 trajectories were run every hour for each 9-hour long filter sampling period starting at a height of 250 m
164 above ground level (agl), which effectively models transport into the marine boundary layer (MBL, with a
165 minimum height of ~500 m over the BUS; Preston-Whyte et al., 1977). This choice also considered the
166 model vertical resolution (23 levels throughout the atmospheric column). The first model vertical level is
167 at 1000 hPa (approximately 110 m amsl) and the next is at 975 hPa (approximately 300 m amsl). The Global
168 Data Assimilation System (GDAS) reanalysis dataset with a 1° x 1° resolution, provided by the National
169 Centre for Environmental Prediction (NCEP), was used. This was preferred to the 0.5° x 0.5° resolution
170 dataset where the vertical velocity is absent and has to be calculated from the divergence, introducing
171 uncertainties into the model. Trajectories were run through the Rstudio interface using the
172 rich_iannone/splitR (available from https://github.com/rich-iannone/ SplitR) and Openair (Carslaw and
173 Ropkins, 2017) packages from the open-source libraries.

174 As a complement, publicly available daily synoptic charts provided by the South African Weather Service
175 (SAWS, www.weathersa.co.za/home/historicalsynoptic; last accessed 20/02/2020) were analysed for the
176 synoptic-scale induced flow.

3. Source identification and apportionment

178 The identification of the origin of the aerosols, complementary to the analysis of the air mass back
179 trajectories and local wind speed and direction, was undertaken by examining the temporal correlations of
180 the elemental and ionic concentrations to known tracers and positive matrix factorisation.

3.1 Ratios to unique tracers

182 The identification and quantification of the aerosol types contributing to the total particle load at HBAO
183 were done by investigating the linear correlation of measured elemental and ionic concentrations and their
184 mass ratios to unique tracers of the atmospheric particulate matter emission sources expected in the
185 region. These are:

186 ● Sea salt aerosols, traced by Na^+ constituting 30.6 % of the aerosol mass in seawater (Seinfeld and
187   Pandis, 2006);
188 ● Marine biogenic emissions during the life cycle of marine phytoplankton in the BUS (Nelson and
189   Hutchings, 1983) and traced by the concentrations of particulate MSA, a unique product of the
190   oxidation of gaseous DMS (Seinfeld and Pandis, 2006);
191 ● Wind-blown mineral dust liberated from the surface of pans and ephemeral river valleys (Annegarn
192   et al., 1983; Eltayeb et al., 1993; Heine and Völkel, 2010; Dansie et al., 2017), but also during /road
193   construction and mining activities (KPMG, 2014). Mineral dust is traced by elemental aluminium,

Atmospheric
Chemistry
and Physics
Discussions

Open Access

EGU

194   representing aluminosilicate minerals and contributing on average 8.13% of the global crustal rock
195   composition by mass (Seinfeld and Pandis, 2006), and by the non-sea salt (nss) fraction of Ca^{2+} to
196   represent calcium carbonate. This is justified by the specific mineralogy of Namibian soils which
197   are enriched in gypsum ($CaSO_4OH$) and calcite ($CaCO_3$), and presenting calcium content higher than
198   the world average (Annegarn et al., 1983; Eltayeb et al., 1993). The apportionment of the sea-salt
199   (ss) and non-sea salt (nss) Ca^{2+} fractions was done using the nominal mass ratio of Ca^{2+}/Na^+ in
200   seawater (0.021; Seinfeld and Pandis, 2006). The evaluation of the mass concentration of calcium
201   carbonate was done by multiplying the measured nss-Ca^{2+} mass concentration by the $CaCO_3/Ca$
202   mass ratio of 2.5;

203   ● Elements such as Ni, V, Pb, Cu, Zn to trace heavy-oil combustion from industry and commercial
204   shipping (Becagli et al., 2017; Johansson et al., 2017; Sinha et al., 2003; Vouk and Piver, 1983) as
205   well as mining activities (Ettler et al., 2011; Kříbek et al., 2018; Soto-Viruet, 2015), and;

206   ● nss-K^+, calculated from measured K^+ assuming the mass ratio K^+/Na^+ of 0.036 as in seawater
207   (Seinfeld and Pandis, 2006), to trace seasonal transport of biomass burning aerosols (Andreae et
208   al., 1998; Andreae and Merlet, 2001).

3.2   Positive matrix factorisation

210   Positive matrix factorization (PMF) multivariate statistical methods are widely used to identify source
211   profiles and explore source–receptor relationships using the trace element compositions of atmospheric
212   aerosols (e.g., Schembari et al., 2014). The PMF uses weighted least-squares factor analysis to deconvolute
213   the matrix of observed values (X) as $X = G$ x $F + E$, where G and F are the matrices representing the factor
214   scores and factor loadings, respectively, and E is the matrix of residuals equal to the difference between
215   observed and predicted values (Paatero and Tapper, 1994; Paatero et al., 2014).

216   In this paper, the multivariate PMF statistical analysis was conducted with the EPA (Environmental
217   Protection Agency) PMF version 5.0 (Norris et al., 2014). The XRF and IC datasets were combined by
218   retaining only elements/ions measured above the MQL in more than 70 samples (that is, at least in 20% of
219   the collected values). This criterion excluded Ba, Br⁻, PO₄⁻ and Mn^{2+}. Occasional missing values in the
220   retained elements/ions were replaced by the species median value, as recommended in Norris et al.,
221   (2014). Uncertainties for all missing values in the dataset were replaced by a dummy value (99999) to
222   ensure that these samples do not skew the model fit (Norris et al., 2014). According to section 5.2.1, the
223   water-soluble ionic form instead of the elemental form was retained for elemental Mg, Na, Cl, K, Ca and S.
224   SO_4^{2-}, K^+ and Ca^{2+} were included as their ss- and nss- fractions. The final matrix was made up of 385
225   observations of 33 chemical species. By comparing the signal to noise ratio, the nss-K+ was the only species
226   in the matrix marked as a "weakBased on the temporal correlation, the PMF analysis resolves the chemical

227   dataset into a user-specified number of solutions (sources). No completely objective criterion exists for

228   selecting the number of sources and so the model was run considering potential solutions of three to seven

229   sources. Each of these models were run 100 times using randomised seeds. For each of these runs, the

230   robustness-of-fit was compared and the estimation of the error range of each solution was done by

231   displacing chemical species in each modelled source and testing the rotational ambiguity of the solutions

232   (Norris et al., 2014; Paatero et al., 2014). *Fpeak* rotations with strengths between -0.5 and 1.5 were tested

233   to further optimise the source solutions. An *Fpeak* strength of 0.5 was used for the final solution. From these

234   analyses, the solution with the smallest uncertainties and greatest stability was selected as the most

235   physically meaningful and representative solution.

236   **4.   Results and discussion**

237   **4.1   Meteorological conditions during sampling**

238   The characteristic synoptic circulation patterns identified over the west coast of southern Africa that are

239   significant for this study include continental-anticyclonic circulation., the southeast Atlantic anticyclone,

240   west coast troughs and barotropic easterly waves, transient baroclinic westerly waves and coastal low-

241   pressure systems (Tyson and Preston-Whyte, 2014). Formenti et al. (2018), found that anticyclonic

242   circulation, both in the form of the South Atlantic anticyclone and the continental anticyclone, is the most

243   persistent circulation patterns over the west coast of Namibia.

244   Figure 2 shows weekly composite maps of calculated air mass back trajectories (their gridded frequency

245   plot is shown in Figure S2). Southerly and south-westerly transport occurred year-round and easterly

246   transport mainly occurred during late autumn (May), winter (June, July and August) and early spring

247   (September, October and November). Large scale north-easterly air mass transport towards HBAO was

248   restricted to the austral autumn and winter when continental anticyclonic flow dominated the circulation

249   patterns in the lower and mid-troposphere. The majority of air masses arriving in the MBL are of marine

250   origin from the southern and south-eastern Atlantic and show the transport of marine air masses toward

251   the subcontinent, divergence at the escarpment and southerly flow, induced along the coast. Most of the air

252   masses were transported over coastal waters offshore and along the west coast of South Africa and Namibia

253   and just inland to the north-northeast of HBAO from the sub-continent. Continental plumes arriving at

254   HBAO are transported easterly between 15° and 22°S and from as far as 36°E.

255   Emissions along these preferred pathways may be of great significance in shaping the regional aerosol

256   background. Some of the known transport regimes are associated with mid-tropospheric easterly winds,

257   responsible for transport off the subcontinent (Swap et al., 1996; Tyson et al., 1996). To the north of HBAO,

258   Adebiyi and Zuidema (2016) observed continental plumes transported off the coast, especially under

259   anticyclonic circulation over the subcontinent and the southeast Atlantic Ocean. Tlhalerwa et al. (2012)

Atmospheric
Chemistry
and Physics
Discussions

Open Access

EGU

260   found berg winds, an easterly perturbation, to be the main agents of aerosol transport and deposition off

261   the coast at Luderitz, around 500 km south of HBAO, and easterly winds in the boundary layer may

262   transport dust from the subcontinent into the ocean.

263   The weekly and hourly variability of local surface winds is illustrated in Figures 2 and 3, respectively. On

264   average the wind is characterised by low speeds during the daytime (4.7 ± 2.2 m s^{-1} with only 0.3% calm)

265   and at night (3.3 ± 2.1 m s^{-1} with 0.6% calm conditions). The low wind speeds are typical for regions

266   frequently experience anticyclonic circulation. The highest wind speeds were recorded for southerly winds

267   which were persistent throughout the sampling period, except during January 2017 (Figure 2). The highest

268   wind speed was recorded in the austral spring in both years and reached a maximum of 18.9 m s^{-1} in the

269   week of 13–20 November 2017.

270   Another feature that is promoted by anticyclonic flow is thermally-induced land and sea breezes. Sea

271   breezes were a common daytime occurrence at HBAO. The sea breeze is typically characterised by

272   southerly and south-westerly winds. The wind direction is partly a function of the shape of the coastline at

273   Henties Bay and the overlying gradient flow. The daytime land breeze was not observed as frequently as

274   the onshore sea breeze flows. This supports the conclusion that the mechanisms for onshore flow are a

275   combination of local and large-scale circulation. ENE and northerly winds were seen in July 2016 reaching

276   a maximum speed of 13 m s^{-1} (mean wind speed of 4.5 ± 2.2 m s^{-1} for the week of 19-26 July 2016). These

277   are the land breezes that are also most likely to develop on clear stable nights. The northerly flow, in

278   particular, occurred in the early evening and mid-morning (Figure 4), with no seasonal dependence.

279   Overall, it is important to note that the sea-breeze winds during the day are well defined in the data. At

280   night the land breeze is much less important at Henties Bay than one might expect at a coastal site. This is

281   almost certainly driven by the small thermal gradient that exists between the ocean and land temperatures

282   at night. In the absence of a well-defined gradient, the land breeze does not develop on most nights.

283   Direct westerly winds occur less frequently at the site. The winds could be observed during the day and the

284   night indicating that they are not exclusively established as sea breeze cells. The wind speeds for westerly

285   flow conditions never exceeded 6 m s^{-1}.

286   Easterly winds were only observed during the warmer months (January to March and September to

287   December, Figure 3), and during the night-time sampling periods (21 to 9 UTC), when their speeds

288   remained below 4 m s^{-1} (Figure 4). This local circulation is driven by easterly wave or tropical easterly

289   circulation that moves southward during the summer months.

4.2   Variability and apportionment of measured concentrations

A summary of the measured elemental and water-soluble mass concentrations (arithmetic mean, standard deviation and range of variability) at HBAO during 2016 and 2017 are provided in Table 1. The time series of the mass concentrations of the source tracers discussed in section 3.1 are shown in Figure 5.

4.2.1   Sea salt

As expected, the major components of sea salt aerosols (Cl^-, Na^+, Mg^{2+} and K^+) were sampled in high concentrations (up to 76, 53, 5.6 and 2.0 µg m^{-3}, respectively) throughout the sampling periods. Their time variability, illustrated in Figure 5 by the example of Na^+, was very similar and characterised by a significant continuous background that could be represented by a 10-point moving average (that is, 90 hours). The calculated mean background concentration was 10.1 ± 3.6 µg m^{-3}. No seasonal cycle was evident due to the dominance of southerly and south-westerly winds transporting marine air masses onshore (Figure 3).

Table 2 shows the mass ratios of Cl^-, Mg^{2+}, K^+, Ca^{2+}, F^- and SO_4^{2-} to Na^+ for 2016 and 2017 calculated as the slopes of their linear regression lines, and evaluated by the coefficient of determination (R^2). The experimental values were compared with average ratios in seawater (Seinfeld and Pandis, 2006). The average Cl^-/Na^+ mass ratio was 1.35 ± 0.11 in 2016 and 1.34 ± 0.11 in 2017, lower by 25% than the value expected in seawater of 1.8. This difference has previously been reported in fresh sea salt in acidic marine environments (e.g., Zhang et al., 2010), and is attributed to Cl^- depletion via reactions between NaCl and sulfuric- and nitric acids. A very good correlation was observed between the ratios of Mg^{2+}(0.12 ± 0.01) and K^+(0.04 ± 0.01) to Na^+ in this data set and the value reported for sea water (Table 2) and, (Seinfeld and Pandis, 2006). Conversely, the linear correlation between Ca^{2+} and Na^+ (not shown) was less pronounced (R^2 = 0.61 and 0.42 in 2016 and 2017, respectively). The Ca^{2+}/Na^+ mass ratio was systematically higher than in seawater (0.04), indicating the contribution of crustal calcium typical of the Namibian soils (see section 4.2.2). Using the average seawater ratio, the mean sea-salt (ss) Ca^{2+} concentration was estimated as 470 ± 360 ng m^{-3} and 360 ± 210 ng m^{-3} for 2016 and 2017, respectively. The mean non-sea-salt (nss) Ca^{2+} concentration was 420 ± 520 and 270 ± 400 ng m^{-3}, respectively for the two years, representing 47% and 42% of the mean measured Ca^{2+} concentrations. Similarly, for both 2016 and 2017, the ss and nss components of K^+ were estimated as 367 ± 246 ng m^{-3} and 44 ± 54ng m^{-3} respectively, accounting for 89 % and 11% of the K^+ mass. Finally, the SO_4^{2-}/Na^+ mass ratio for HBAO (0.36 ± 0.14) was higher than the average mass ratio for seawater (0.25). The origin and significance of this excess are explored in section 4.2.6.

4.2.2   Mineral dust

The time series of Al and nss-Ca^{2+} (Figure 5) were investigated to identify the transport of airborne mineral dust at Henties Bay. Mineral dust episodes were identified when the concentrations of those tracers

323   exceeded background values (modelled as the 10-point moving average) for a minimum of 3 consecutively

324   sampled filters. Similar time variability was observed for elemental Fe, Si, Ti and P (not shown). Overall, 19

325   episodes of mineral dust were identified (Table S1).

326   The mean mass concentration of elemental Al was 556 ± 643 ng m^{-3} in 2016 and 446 ± 551 ng m^{-3} in 2017,

327   while values peak as high as 4.7 µg m^{-3} (Table 1). To the best of our knowledge, no other measurements of

328   Al are available in Namibia for comparison. Our nss-Ca^{2+} mean (703 ± 644 ng m^{-3} in 2016 and 428 ± 437 ng

329   m^{-3} in 2017) is similar to the concentrations measured by Annegarn et al. (1983)(425 ng m^{-3} and maximum

330   of 800 ng m^{-3}) in central Namibia at Gobabeb, in the Namib Desert, (23°45'S, 15°03'E). The annual mean Fe

331   concentration measured at HBAO (372 ± 480 ng m^{-3} in 2016 and 338 ± 433 ng m^{-3} in 2017) compares well

332   with the average of 246 ng m^{-3} provided by Annegarn et al. (1983).

333   Table 3 shows the mass ratios for major components of mineral dust as well as some heavy metals (V and

334   Ni). Overall, Si, Fe, and Ti showed very good correlations to Al as expected for mineral dust ($R^2 > 0.9$). The

335   average mass ratio of Si/Al was 3.7 ± 1.0 in 2016 and 3.3 ± 0.9 in 2017, lower than the average values of 4

336   to 4.6 expected in global soils and crustal rock (Seinfeld and Pandis, 2006). This is attributed to the size-

337   fractionation during aeolian erosion of soils producing airborne dust. As a matter of fact, our average values

338   are consistent with those obtained for particles less than 10 µm in diameter by Eltayeb et al. (1993) at

339   Gobabeb. Our averages, generally higher than in mineral dust from north Africa (Formenti et al., 2014),

340   compare well with the value (3.4) reported by Caponi et al. (2017) for mineral dust aerosols generated in

341   a laboratory experiment from a soil collected to the northeast of HBAO. The average Fe/Al ratio was $0.7 \pm$

342   0.2 in 2016 and 0.8 ± 0.04 in 2017, lower than the ratio of 1 reported by Eltayeb et al. (1993). The same is

343   observed for the Ti/Al ratio, which was 0.07 ± 0.02 in 2016 and 0.06 ± 0.03 in 2017 at HBAO and

344   approximately 0.15 in Eltayeb et al. (1993).

345   The average nss-Ca^{2+}/Al ratio was 1.6 ± 0.7 in 2016 and 1.4 ± 0.7 in 2017. However, for the strongest dust

346   episodes (Al values higher than 1 µg m^{-3}) the ratio tended to 1 (Figure 6). This is in agreement with the

347   specific mineralogy of Namibian soils that are rich in limestone and gypsum (Annegarn et al., 1983; Eltayeb

348   et al., 1993). The mean Fe/nss-Ca^{2+} ratio was 0.5 ± 0.2 in 2016 and 0.7 ± 0.2 in 2017, higher than the value

349   of 0.11 ± 0.10 reported by Caponi et al. (2017), pointing to the diversity in soil mineralogy, even at relatively

350   small spatial scales.

351   Figure 6 also shows the nss-K$^+$/Al ratios as a function of Al. As for nss-Ca^{2+}, values were spread but ranged

352   between 0.1 and 0.5 when Al concentrations exceeded 1 µg m^{-3}. These values are in agreement with those

353   for mineral dust sources in North Africa (Formenti et al., 2014).

Atmospheric
Chemistry
and Physics
Discussions

Open Access

EGU

354 The average phosphorus concentrations measured at HBAO were 11 ± 9 ng m^{-3} in 2016 and 14 ± 4 ng m^{-3}

355 in 2017. Phosphorous was very well correlated with Al in 2016 (R^2 = 0.92) and only moderately correlated

356 in 2017 (R^2 = 0.66). The P/Al ratio averaged 0.03 ± 0.02 in 2016 and 0.05 ± 0.02 in 2017. As was observed

357 for the nss-Ca^{2+}/Al, the P/Al ratio tended to an asymptotic value of 0.02 when Al exceeded 1 µg m^{-3} (not

358 shown). This is significantly higher than reported by Formenti et al. (2003a) for the outflow of Saharan dust

359 to the North Atlantic Ocean (0.0070 ± 0.0004).

360 The mean concentrations of mineral dust elements Al, Fe, Ti and Si were higher for night-time sampling

361 between 21 and 06 UTC, and lower in the day (9 to 18 UTC). It follows that the local measurement of easterly

362 winds was only observed at night and in the early morning (Figure 4), consistent with these higher

363 concentrations in mineral dust elements.

364   ### 4.2.3 Heavy metals

365 Vanadium and nickel are naturally occurring in mineral deposits in soils (Annegarn et al., 1983; Maier et

366 al., 2013), but they are also known tracers of heavy-fuel combustion, as reported in Becagli et al. (2013)

367 and references therein. Their average concentrations at HBAO were 9 ± 5 ng m^{-3} (2016) and 7 ± 6 ng m^{-3}

368 (2017) for V, and 8 ± 7 ng m^{-3} (2016) and 7 ± 4 ng m^{-3} (2017) for Ni. These values are an order of magnitude

369 larger than measured over the open ocean by Chance et al. (2015) and comparable to those measured by

370 Isakson et al. (2001) at a Swedish harbour and by Becagli et al. (2012) in the central Mediterranean Sea

371 downwind of a major shipping route. In our study, V and Ni were relatively well correlated. Vanadium was

372 well correlated with Al when Al exceeded 1 µg m^{-3} (R^2 around 0.4), whereas no correlation between Ni and

373 Al were observed (Figure 6). Additionally, the correlation of V to Si, also used in the literature as a tracer of

374 mineral dust, was evident while moderate (R^2 around 0.4), while none was found for Ni. This differs from

375 what was reported by Becagli et al. (2012), who found that neither V nor Ni were correlated to Si. In our

376 dataset, both V/Si and Ni/Si ratios were enriched by a factor of 10 or more to reference values for the upper

377 continental crust (3.1×10^{-4} and 1.5×10^{-4} for V/Si and Ni/Si, respectively; Henderson and Henderson, 2009).

378 The highest V concentrations corresponded to south-south-easterly winds while the highest Ni

379 concentrations were found for southerly to westerly winds.

380 These facts, and the moderate to good correlations of V and Ni with Zn, Cu and Pb, suggest that V and Ni do

381 not necessarily have the same sources. Mining activities, likely in the Otavi mountain area (Boni et al.,

382 2007), should account for the high concentrations of V, with additional contributions from combustion of

383 heavy fuels, where V is present as an impurity (Isakson et al., 2001, and references therein; Vouk and Piver,

384 1983). On the contrary, combustion of heavy fuels seems to be the primary source of Ni. Indeed, HBAO is

385 located downwind one of the major ship tracks of southern Africa (Tournadre, 2014). The V/Ni ratio for

386   2016 is 1.7 ±1.1 and 2017 is 1.3 ± 1.3, lower than 2.8-2.9 reported for the central Mediterranean (Becagli

387   et al., 2017) and 4-5 reported for a harbour in Melilla, Spain (Viana et al., 2009).

388   Zn and Pb are also found as impurities in bulk fuels for ships (Isakson et al., 2001). The mean concentration

389   of Zn at HBAO (11 ± 9 ng m^{-3}) was about two orders of magnitude higher than over the southeast Atlantic

390   Ocean (Chance et al., 2015) and in desert air (Annegarn et al., 1983). Likewise, the mean Pb concentration

391   (75 ± 89 ng m^{-3}) was three orders of magnitude higher than reported by Chance et al. (2015) for soluble Pb

392   and comparable to values measured in the western Mediterranean by Denjean et al. (2016). Average

393   concentrations of Cu at HBAO were 8 ± 6 ng m^{-3}, an order of magnitude higher than measured in windblown

394   dust by Annegarn et al. (1983) in the central Namib but two orders of magnitude smaller than the average

395   measured by Lee et al. (1999) in highly polluted Hong Kong (125.1 ng m^{-3}). Ettler et al. (2011) showed that

396   copper ore mining and smelting operations in the Zambian Copperbelt are a significant source of potentially

397   bioavailable copper, that, unlike phosphorus, has been found to inhibit plankton growth in laboratory

398   studies (Paytan et al., 2009) and over the western Mediterranean (Jordi et al., 2012). Similar contamination

399   of topsoil was found by Kříbek et al. (2018) at operations in the Tsumeb mining district, Namibia (19°14'S,

400   17°43'E).

4.2.4   Fluoride

402   Atmospheric fluoride is primarily from fluorspar mining in the Okorusu Mine (20°3'S, 16°44'E), but very

403   likely also from the surface mining occurring approximately 20 km south of HBAO to provide gravel for the

404   construction of a major road between Swakopmund and Henties Bay which started late in 2015 (A.

405   Namwoonde, *pers. corr.*). Fluoride may be leached into groundwater from fluoride-rich soils throughout

406   the region (Wanke et al., 2015), which may then evaporate when exposed to the atmosphere.

407   One of the striking features of Table 1 is the high mean concentration of F$^-$ measured at HBAO (4.3 ± 4.0 µg

408   m^{-3} in 2016 and 2.8 ± 2.5 µg m^{-3} in 2017), with peak values as high as 25 µg m^{-3}. Those annual mean

409   concentrations were comparable to the mean 24-h fluoride concentrations measured between 1985 and

410   1990 over the South African Highveld by Scheifinger and Held (1997). The peak values at HBAO were

411   significantly higher than maxima reported by these authors and ranging between 1.4 and 2.9 µg m^{-3}. The

412   measured concentrations at HBAO were also comparable to those of heavily polluted areas in China (Feng

413   et al., 2003), and significantly higher than reported for Europe, even in the polluted Venice lagoon (Prodi et

414   al., 2009) or in areas nearby ceramic and glass factories (Calastrini et al., 1998). The mean F$^-$/Na$^+$ mass ratio

415   measured at HBAO was 0.39 ± 0.29 in 2016 and 0.32 ± 0.29 in 2017, enriched by several orders of

416   magnitude to average seawater composition (mass ratio 1.2x10^{-4}; Table 2). The very good correlation of F$^-$

417   with nss-Ca^{2+} (R^2 equal to 0.76 in 2016 and to 0.84 in 2017) yielded a mean mass ratio of 6.4 and 5.8,

418   respectively,   much   higher   than   reported   in   groundwater,   aerosols   or   precipitation   in   polluted

419   environments (Feng et al., 2003; Prodi et al., 2009). The highest F⁻ concentrations were associated with

420   south to the easterly winds, that is, from the subcontinent.

4.2.5   Arsenic

422   Inorganic arsenic in geologic formations may be released by mining operations or evaporated from soil and

423   groundwater (Gomez-Caminero et al., 2001). No correlation between As to Al nor nss-Ca^{2+} was found.

424   Arsenic is also released by marine algae and plankton (Sanders and Windom, 1980; Shibata et al., 1996).

425   Again, no discernible correlation between As and MSA was found. Other sources of arsenic are biomass

426   burning, fossil fuel combustion and non-ferrous metal smelting operations (Ahoulé et al., 2015; Gomez-

427   Caminero et al., 2001). The arsenic concentrations at HBAO have a mean and standard deviation for 2016

428   of 22 ± 16 ng m⁻³ and 239 ± 344 ng m⁻³ in 2017. The mean for 2017 is skewed due to two sampling weeks

429   with very high concentrations in the order of those measured in rural and urban-industrial areas affected

430   by mining and smelting emission sources (Hedberg et al., 2005; Šerbula et al., 2010). For these two weeks,

431   the MSA concentrations were slightly higher than the mean reported in Table 1 (77 ± 33 ng m⁻³) as were

432   the Sr concentrations (146 ± 53 ng m⁻³). This may indicate contributions during these two weeks from

433   marine biogenics and/or from the Tsumeb smelter in the northeast of HBAO (KPMG, 2014).

4.2.6   Sulphate and secondary aerosols

435   The annual mean sulphate concentration measured at HBAO was 4.1 ± 2.6 µg m⁻³ in 2016 and 3.4 ± 1.4 µg

436   m⁻³ in 2017 (Table 4), higher than previously measured over the southern Atlantic and Pacific oceans

437   (Zhang et al., 2010) and comparable to springtime measurements in the Venice Lagoon (Prodi et al., 2009).

438   As shown in Formenti et al. (2019), the highest concentrations were measured in spring and autumn, while

439   minima occurred between May and August. SO_4^{2-} and Na^+ showed good correlation (R^2 = 0.92 in 2016 and

440   0.83 in 2017, Table 2) but their mass ratios were higher than in seawater (0.36 ± 0.14 and 0.42 ± 0.23 in

441   2016 and 2017, respectively, compared to the expected mass ratio of 0.25; Seinfeld and Pandis, 2006). The

442   apportionment of the ss and nss fractions of SO_4^{2-} was done using the nominal mass ratio of SO_4^{2-}/Na^+ in

443   seawater (0.25; Seinfeld and Pandis, 2006). As a result, up to 57% of the measured SO_4^{2-} mass concentration

444   in the PM_{10} fraction was attributed to sea salt aerosols, and the nss-component was of the order of 43%.

445   This is in agreement with previous observations in the south Atlantic Ocean (Andreae et al., 1995; Zhang et

446   al., 2010; Zorn et al., 2008). On the contrary, at the remote Brand se Baai site along the Atlantic coast of

447   South Africa (31.5°S 18°E), Formenti et al. (1999) reported than sea salt accounted for about 92% of the

448   total measured elemental sulphur concentrations.

449   The MSA concentrations measured at the site ranged between 10 and 230 ng m⁻³ (Table 1). The mean

450   annual concentration was 63 ± 39 ng m⁻³, three times higher than the mean value of 20 ± 20 ng m⁻³ (6.2 ±

451   4.2 ppt) reported by Andreae et al. (1995) over the open ocean along 19°S, and lower than in the southeast

452   Atlantic Ocean (Zhang et al., 2010; Table 4). As shown by Formenti et al. (2019), the MSA concentration at

453   HBAO displayed a clear seasonal cycle, with higher values in spring to summer, as previously observed in

454   the Southern Hemisphere ocean due to more efficient oxidation of DMS in warmer conditions (Ayers et al.,

455   1997; Huang et al., 2017). This also explains the highest mean concentrations of marine biogenic products

456   (MSA, As and nss-SO_4^{2-}) measured in the morning and the lowest at night. Springtime averages for MSA

457   were in the range of that measured by Huang et al. (2018) during a springtime cruise over the South Atlantic

458   and by Prodi et al. (2009) in the Venice Lagoon (Table 4).

459   The MSA/nss-SO_4^{2-} ratio (Figure 7) displayed a large range of values (0.01 to 0.12), in agreement with

460   values in the literature at various geographical locations, especially in the southern Hemisphere (Table 4).

461   As pointed out by Formenti et al. (2019), the MSA/nss-SO_4^{2-} values were higher in the austral summer and

462   spring and lower in the austral winter. This strong seasonal dependence is in agreement to that identified

463   by Ayers et al. (1986) for marine biogenic sulphur in the Southern Hemisphere and suggests that the highest

464   concentrations of nss-SO_4^{2-} in the PM_{10} (nss-SO_4^{2-} larger than 2 µg m^{-3}) are not necessarily associated to

465   marine biogenic emissions. From measurements at the desert station of Gobabeb, in the Namib Desert,

466   Annegarn et al. (1983) found that only the fine mode of the bimodal distribution of sulphur aerosols, that

467   is, that bearing the lower mass concentrations, would be due to the oxidation of sulphur-containing gaseous

468   emissions during the marine phytoplankton life cycle.

469   Figure 7 also illustrates the NH_4^+/nss-SO_4^{2-} mass ratio as a function of nss-SO_4^{2-} mass concentrations. Both

470   in 2016 and 2017, the NH_4^+/nss-SO_4^{2-} mass ratios were less variable than for MSA/nss-SO_4^{2-}. The annual

471   mean NH_4^+/nss-SO_4^{2-} were 0.13 ± 0.10 in 2016 and 0.14 ± 0.08 in 2017. These values are consistent with

472   the mass ratio of 0.18 corresponding to ammonium bisulphate ((NH_4)HSO_4). Although some losses of NH_4^+

473   due to conservation on-site and transport to the laboratory in France cannot be excluded, the measured

474   ratios are consistent with previous investigations in remote marine environments reported in Table 4,

475   including offshore southern Africa (Andreae et al., 1995; Quinn et al., 1998).

476   The average NO_3^-/nss-SO_4^{2-} ratio at HBAO was of the order of 0.14, significantly smaller than reported by

477   Zhang et al. (2010) over the southeast Atlantic. Finally, poor correlation between nss-SO_4^{2-} and nss-Ca^{2+}

478   (not shown) suggests that very little of the sulphate is present as $CaSO_4$, either formed by heterogeneous

479   deposition of SO_2 on calcite mineral particles or liberated from the soils as mineral gypsum (Annegarn et

480   al., 1983).

481   Finally, the mean annual concentration of oxalate at HBAO was 72 ± 80 ng m^{-3} in 2016 and 141 ± 50 ng m^{-3}

482   in 2017. Values at HBAO are consistent with those reported by Zhang et al. (2010) over the southeast

483   Atlantic (200 ± 140 ng m^{-3}). Oxalate aerosols in the atmosphere are due to marine biogenic activity and

484 anthropogenic emissions including fossil fuel combustion and biomass burning (Gillett et al., 2007, and

485 references therein). It is also formed by in-cloud processes and oxidation of gaseous precursors followed

486 by condensation (Baboukas et al., 2000). The moderate correlation with NO_3^-, $nss-SO_4^{2-}$ and $nss-K^+$,

487 particularly in 2017, could suggest a common origin and possible influence of occasional biomass burning.

488 ### 4.3   Source apportionment

489 Figure 8 presents a summary of the five source profiles resolved by the selected PMF solution. According

490 to their characteristic tracers, the five sources are labelled sea salt (Na^+, Cl^-, F^-, Mg^{2+}, $ss-SO_4^{2-}$, $ss-K^+$ and $ss-$

491 Ca^{2+}), marine biogenic (MSA, oxalate and As), mineral dust (Si, Al, Fe, Ti, F^-, $nss-K^+$ and $nss-Ca^{2+}$), secondary

492 products ($nss-SO_4^{2-}$, NH_4^+, formate, oxalate and $nss-K+$) and heavy metals (V, Ni, Zn, Pb, Cr, Cu, Cd, Nd, Sr

493 and Co). For the sake of comparison, the mass concentration of sea salt and mineral dust can also be

494 evaluated from the chemical composition as:

495   [Sea salt] = 2.57 *[Na^+], as in Zhang et al. (2010)   (1a)

496   [MD] = [Mineral dust] = [Al]/0.0813 + 2.5 * [$nss-Ca^{2+}$], as explained in section 3.1   (1b)

497 The estimated aerosol mass (EAM) needed to evaluate their percent contributions can then be calculated

498 as:

499   [EAM] = [Sea salt] + [Mineral dust] + [other]   (1c)

500 Where [other] represents the major compounds (by mass) in the input dataset, as:

501   [other] = [V]+[Ni] + [Zn] + [Pb] + [Cr] + [Cu] + [$nss-SO_4^{2-}$] + [NH_4^+] + [MSA] + [NO_3^-] + [Oxalate]   (1d)

502 #### 4.3.1   Sea salt

503 Due to the location of the sampling site in this windy, coastal region, sea salts were present to some extent

504 in all the PMF resolved sources. The sea salt source profile is described by typical elements like sodium,

505 chloride, fluoride and magnesium ions as well as the sea salt fraction of potassium, sulphate and calcium

506 (Figure 8). These species accounted for 70.8 ± 0.2% of the total estimated mass concentration, in good

507 agreement with the percent contribution of the sea salt mass from Equation 1a (70.4%). In general terms,

508 the source profile obtained by PMF is in good agreement with that obtained by chemical apportionment. In

509 particular, the Cl^-/Na^+ mass ratio is 1.4 ± 1.6, confirming the depletion of Cl^- with respect to Na^+. The mass

510 ratio of 0.11 ± 0.01 for Mg^{2+}/Na^+ estimated in this source was in good agreement to that reported in Table

511 2 and for the average seawater composition. The F^-/Na^+ mass ratio reported in Table 2 is higher than 0.19

512 ± 0.12 for this PMF sea salt source and this ratio is still two orders of magnitude higher than the average

513 seawater composition reported in Seinfeld and Pandis (2006).

514   A separate PMF analysis was run with Ca^{2+}, SO_4^{2-} and K^+ ions without separating the sea salt from non-sea

515   salt components. The contributions of these elements to the sea salt aerosol mass were estimated to be 55

516   ± 0.1% of the calcium, 60.1 ± 0.1% of the sulphate and 72.9 ± 0.1% of the potassium. This compared well to

517   the PMF solution of the dataset with the species separated by ss and nss components, indicating good

518   agreement in the apportionment by nominal mass ratios and PMF of the sea salt source.

519   4.3.2   Marine biogenic

520   The marine biogenic source profile contributed 13.5 ± 0.8% to the PM_{10} mass concentration. The source

521   profile is composed of secondary products emitted by marine biogenic processes such as MSA, oxalate and

522   As (Figure 8), which however only account for 2.8% (± 0.1%) of the total mass. The largest fraction of the

523   mass is contributed by Cl^- and Na^+ (combined mass contribution of 67.3 ± 0.1%) and ss- and nss-sulphates

524   (12.7 ± 0.1%). The MSA/nss-SO_4^{2-} mass ratio for this source is 0.05 ± 0.25 and compares well to the chemical

525   apportionment and what was measured in the region by Andreae et al. (1995).

526   The fact that we find arsenic in this source is interesting, as it was not immediately evident from the analysis

527   of correlations between the two, but it does confirm the contributions from marine biogenic sources

528   (Sanders and Windom, 1980; Shibata et al., 1996).

529   4.3.3   Mineral dust

530   The contribution of mineral dust to the PM_{10} aerosol mass estimated by the PMF analysis is 9.9% (± 0.1%),

531   lower than the average of 17% calculated with Equation 1b. The difference in the estimated aerosol mass

532   is then likely explained by the use of the average aluminium content in global soils (8.13%) in the

533   calculation of estimated aerosol mass, indicating a significant difference in aluminium content of Namibian

534   soil as compared to the global average.

535   The mineral dust source profile was composed by Si, Al, Fe, Ti, F^-, nss-K^+ and nss-Ca^{2+} (Figure 8), accounting

536   for almost all of its evaluated mass concentration (94.9 ± 0.1%). The mass contributions of P, Mn and V to

537   the source profile was small (0.3± 0.1%). Nevertheless, mineral dust accounts for up to 40 to 55% of their

538   variance in mass. The vanadium in this source was highly enriched to the nickel in the V/Ni mass ratio of

539   32.74 ± 0.01, not consistent with shipping emissions reported for the Mediterranean (Becagli et al., 2017;

540   Viana et al., 2009).

541   The nss-K^+/Al mass ratio was estimated as 0.07 ± 0.10, lower than that obtained by chemical

542   apportionment (0.13 ± 0.12) and those reported in the literature (0.25 – 0.45, Eltayeb et al., 1993). The PMF

543   allocated 71.4 ± 0.1% of the nss-K^+ to this source and the remaining 28.4 ± 0.1 % to the marine biogenic

544   and secondary products sources.

545   The nss-SO_4^{2-}/nss-Ca^{2+} mass ratio was found to be 0.25 in both the PMF resolved source and the chemical

546   apportionment and was an order of magnitude lower than the mass ratio for gypsum indicating that

547   gypsum was not a main sulphate component in the region. The PMF attributed 35.8 ± 0.1% of the total Ca^{2+}

548   mass to this source, slightly lower than that calculated by nominal mass ratios for the nss-Ca^{2+}(45%). Some

549   very high concentrations in fluoride were associated with calcium and indicate a likely source of calcium

550   fluoride minerals such as fluorspar, presently mined at Okorusu mine.

4.3.4   Secondary products

552   The secondary products source profile, with an estimated PM_{10} aerosol mass of 3.2 ± 1.0%, was identified

553   by secondary nss-SO_4^{2-}, NH_4^+ and formate (Figure 8). These species account for 61.6 ± 0.3% of the source

554   mass. MSA, nitrate, oxalate and nss-K^+ contribute between 15 and 30% of their masses to this source and

555   together account for an additional 17.2 ± 0.1% of the source mass.

556   The NH_4^+/nss-SO_4^{2-} mass ratio for this source was 0.23 ± 0.33, consistent with ammonium bisulphate.

557   Sources of nss-SO_4^{2-} and NH_4^+ include gaseous precursors released from various biogenic and

558   anthropogenic sources, including biomass burning (Andreae et al., 1995; Behera et al., 2013; Theobald et

559   al., 2006; Zhang et al., 2010). The fact that formate, released by the oxidation of DMS and also during

560   biomass burning (Finlayson-Pitts and Pitts Jr, 2000, and references therein) was contributed to this source

561   was not surprising as it is only stable in high concentrations of ammonia (Andreae, 2000). The

562   corresponding contribution of nitrate, oxalate and nss-K^+ to this source might suggest a biomass burning

563   source (Andreae et al., 1998; Andreae and Merlet, 2001; Gillett et al., 2007), but the oxalate/nss-SO_4^{2-} and

564   nss-K^+/nss-SO_4^{2-} for this source were lower than the values reported for biomass burning emissions in

565   Formenti et al. (2003b) and Andreae et al. (1998).

566   The MSA/nss-SO_4^{2-} mass ratio for this source was 0.03 ± 0.02, inconsistent with other literature on marine

567   biogenics reported in Table 4, as opposed to the marine biogenic source identified by PMF which is in good

568   agreement with the ratio reported in Andreae et al. (1995).

4.3.5   Heavy metals

570   The fifth and final source profile (2.3 ± 2.5% to the total mass), was characterised by the heavy metals V,

571   Ni, Zn, Pb, Cr, Cu, Cd, Nd, Sr and Co which together contribute to 34.1 ± 0.8% of the source mass. Sea salt

572   species contributed 68.4 ± 0.2% of the mass of this source. Some of these metals were associated with

573   mineral dust and the additional portions of these metals may be contributed by commercial shipping or

574   industrial processes, as discussed previously. The V/Ni ratio for this source was 1.00 ± 1.00, lower than the

575   average ratios of 1.7 ± 1.1 in 2016 and 1.3 ± 1.3 in 2017 from the chemical apportionment and lower than

576   2.8 – 5 reported for different locations across the Mediterranean (Becagli et al., 2017; Schembari et al.,

577   2014; Viana et al., 2009).

578   Small amounts of nss-SO_4^{2-} were contributed to this source and the nss-SO_4^{2-}/V mass ratio was 23.5 ± 1.75,

579   in good agreement with 16 – 24 reported by Alföldy et al., (2013) for Rotterdam harbour. Although some

580   of these heavy metals may be sourced from the commercial shipping route offshore, the mass ratios for

581   tracer elements were not in agreement with our results and so we cannot conclusively state shipping fuel

582   combustion as the source of these heavy metals.

583   **5. Conclusions and significance of results**

584   This paper presented the first long-term characterisation of the elemental and ionic composition of

585   atmospheric aerosols and the source apportionment of the PM_{10} mass fraction at the Henties Bay Aerosol

586   Observatory on the west coast of southern Africa, an under-explored region of the world to date.

587   The study was based on semi-continuous filter sampling at the HBAO site in Namibia in 2016 and 2017,

588   laboratory analysis of the collected samples by X-ray fluorescence and ion chromatography, and PMF

589   apportionment, supported by back-trajectory calculations and the analysis of local winds.

590   Trajectory analysis for the sampling period from 2016 to 2017 shows four distinct patterns of atmospheric

591   transport to HBAO. Two transport pathways are from the South Atlantic Ocean, namely directly from the

592   east and the south and south-east. A third transport pathway shows air masses reaching Henties bay from

593   the north-west. This pathway will likely include constituents that originated over the continent. The final

594   transport pathway is from central southern Africa.

595   Local wind circulation is influenced by the overlying synoptic circulation patterns as well as local sea breeze

596   mechanisms. Surface flow to HBAO is predominantly from the south and south-west. Southwesterly flow is

597   likely to be linked to sea breeze circulation as a result of thermal gradients in the daytime between the

598   desert surface and the ocean. Land and sea breezes are not common at HBAO due to a weak thermal

599   gradient at night between the ocean and desert surface.

600   In general terms, the results presented in this paper are in fair agreement with the expectations for remote

601   marine regions of the world, and previous observations in the area (Andreae et al., 1995; Zhang et al., 2010).

602   The PM_{10} aerosol load is dominated by natural species such as sea salt, mineral dust and marine biogenic

603   emissions, accounting for more than 90% of the mass. As a consequence of the proximity to the seashore of

604   the HBAO sampling station, the majority of the PM_{10} mass concentration (70%) is due to sea spray, which

605   is persistent at the diurnal and seasonal time scales.

606   For the first time, the frequency, intensity, and elemental composition of Namibian mineral dust aerosols
607   were investigated. Nineteen episodes of increased Al and nss-Ca^{2+} concentrations and lasting from one to a
608   maximum of four days were detected during the entire sampling period. This corresponds well to the
609   frequency of emission of dust plumes from river valleys, coastal sabkhas, and paleo-lacustrine sources
610   (Etosha and Makgadikgadi pans) observed by various authors (Eckardt and Kuring, 2005; Vickery et al.,
611   2013; Dansie et al., 2017). Our data series does not show any particular time dependence of the frequency
612   nor duration of the detected episodes. This is in contrast with the observation by Dansie et al. (2017) that
613   windblown dust derived from the ephemeral river valleys is transported offshore during large easterly
614   wind events, and indicative of the fact that HBAO is the receptor of mineral dust emitted by various sources.

615   One of the striking findings of this paper was the level of anthropogenic contamination and the
616   concentrations of various pollutants, including heavy metals and fluoride. Formenti et al. (2018) already
617   demonstrated a seasonal increase in the light-absorbing carbon particulate between May and late July,
618   indicative of the surface transport of biomass burning aerosols, and episodically throughout the year,
619   attributed to pollution by ship traffic along the Cape of Good Hope sea route. This work additionally
620   demonstrates that mining activities severely affect the air quality and contribute to concentrations as high
621   as, or even higher than in well-known polluted regions of the world, such as the Venice lagoon (Prodi et al.,
622   2009). The persistence of these high concentrations over the two years of sampling is extremely worrying
623   for the affected populations and needs to be addressed by dedicated investigations and decision-making
624   procedures. We suspect that some of that contamination, contributing to the highest heavy metal
625   concentrations in October 2016, might be due to the major road construction between Walvis Bay, past
626   Henties Bay and towards Angola, that started in the second half of 2016. Having said this, despite maximum
627   concentrations being measured at that time, there is no significant difference between the concentration
628   levels in 2016 (before road works) and 2017 (during the road works), suggesting that the pollution by
629   heavy metals is a specific feature in the region, which likely has implications on weather and climate. One
630   such effect could be the deposition of these metals in the ocean. While the deposition of nutrients from the
631   outflow of mineral dust could be important in fertilising waters near the coast (Dansie et al., 2017) and in
632   the Southern Ocean (Okin et al., 2011), the deposition of the trace metals (Cr, Cu, Ni, Mn, or Zn) in aerosols,
633   which play a biological role in enzymes and as structural elements in proteins (Morel and Price, 2003),
634   could also affect the marine productivity of the BUS, one of the most productive marine environments in
635   the world, and should be explored. The complexity and diversity of sources that might contribute to the
636   mineral dust load at HBAO over a year, as well as the detailed chemical composition including trace metal
637   contamination, deserve certainly further dedicated investigation.

638   The long-term time series of aerosol composition at HBAO also provides new and important insights on the

639   contribution of marine emission to the regional aerosol load. Our sampling provides the first long-term

640   measurements of the mass concentrations of MSA in the south Atlantic, and the apportionment of sulphate

641   aerosols, which are important for light scattering and cloud formation. Our data show that sea salt

642   contributes, on average, to around 57% of the total sulphate mass. The non-sea salt fraction (nss-SO_4^{2-}), of

643   the order of 43%, is partly attributed to the oxidation of sulphur-containing gaseous emissions (DMS, SO_2,

644   H_2S) during the marine phytoplankton life cycle, likely favoured by night-time fog and overall elevated

645   relative humidity, typical along the coast. However, nss-SO_4^{2-} mass concentrations over 2 μg m^{-3} could be

646   contributed by ship plumes as well as by episodic biomass burning. Ammonium bisulfate ((NH_4)HSO_4) was

647   found to be the predominant sulphate forms at HBAO, where, incidentally, we observed dramatic rusting

648   and corrosion of materials through the years. The ongoing data analysis of the AEROCLO-sA field campaign

649   will provide with further insights on the size-dependent apportionment, chemical composition and

650   hygroscopicity of sulphate aerosols.

651   ***Data availability.*** Original and analysed data can be obtained by email request to the corresponding author. The

652   SplitR package is found in Iannone (2018). The openair package for R is found in Carslaw and Ropkins (2017). The

653   EPA (Environmental Protection Agency) PMF version 5.0 software is available from https://www.epa.gov/air-

654   research/positive-matrix-factorization-model-environmental-data-analyses. The NOAA Air Resources Laboratory

655   (ARL) provides the HYSPLIT transport and dispersion model and/or READY website (http://www.ready.noaa.gov).

656   ***Author contributions.*** DK, PF, SJP, AN, MC, and AF performed the filter sampling and operated the wind sensor. PH,

657   SC, FL, CMB, ST, and ZZ performed the XRF and IC analysis of the collected samples. DK performed the back-trajectory

658   calculations, analysis of wind data and PMF. DK and PF performed the analysis of the chemical analysis and integration

659   of the dataset. DK and PF wrote the paper with contributions from SJP.

660   ***Competing interests.*** The authors declare that they have no conflict of interest.

661   ***Special issue statement***. This article is part of the special issue "New observations and related modelling studies of

662   the aerosol–cloud–climate system in the Southeast Atlantic and southern Africa regions (ACP/AMT inter-journal SI)".

663   It is not associated with a conference.

References

672

673 Adebiyi, A.A., and Zuidema, P.: The role of the southern African easterly jet in modifying the southeast
674   Atlantic aerosol and cloud environments, Q. J. R. Meteorol. Soc., 142(697), pp. 1574–1589,
675   doi:10.1002/qj.2765, 2016.

676 Ahoulé, D.G., Lalanne, F., Mendret, J., Brosillon, S. and Maïga, A.H.: Arsenic in African Waters: A Review,
677   Water. Air. Soil Pollut., 226(9), doi:10.1007/s11270-015-2558-4, 2015.

678 Alföldy, B., Balzani Lööv, J., Lagler, F., Mellqvist, J., Berg, N., Beecken, J., Weststrate, H., Duyzer, J., Bencs, L.,
679   Horemans, B., Cavalli, F., Putaud, J.-P., Janssens-Maenhout, G., Pinter Csordas, A., Van Grieken, R.,
680   Borowiak, A., Hjorth, J.: Measurements of air pollution emission factors for marine transportation.
681   Atmos. Meas. Tech. 6 (7), pp. 1777 – 1791, doi: 10.5194/amt-6-1777-2013, 2013.

682 Andreae, T.W., Andreae, M.O. and Schebenske, G.: Biogenic sulfur emissions and aerosols over the tropical
683   South Atlantic 1. Dimethylsulfide in seawater and in the atmospheric boundary layer, J. Geophys. Res.,
684   99, pp. 22819-22829, doi: 10.1029/94JD01837, November 20, 1994.

685 Andreae, M.O., Elbert, W. and de Mora, S.J.: Biogenic sulfur emissions and aerosols over the tropical South
686   Atlantic: Atmospheric dimethylsulfide, aerosols and cloud condensation nuclei, J. Geophys. Res. Atmos.,
687   100(June), pp. 11335–11356, doi:10.1029/94JD02828, 1995.

688 Andreae, M.O., Andreae, T.W., Annegarn, H., Beer, J., Cachier, H., Canut, P., Elbert, W., Maenhaut, W., Salma,
689   I., Wienhold, F.G., Zenker, T. and Planck, M.: Airborne studies of aerosol emissions from savanna fires in
690   southern Africa: 2. Aerosol chemical composition, 103(D24), pp. 119–128, doi:10.1029/98JD02280,
691   1998.

692 Andreae, M.O., Elbert, W., Gabriel, R., Johnson, D.W., Osborne, S. and Wood, R.: Soluble ion chemistry of the
693   atmospheric aerosol and SO2 concentrations over the eastern North Atlantic during ACE-2, Tellus, Ser.
694   B Chem. Phys. Meteorol., 52(4), pp. 1066–1087, doi:10.1034/j.1600-0889.2000.00105.x, 2000.

695 Andreae, M.O. and Merlet, P.: Emission of trace gases and aerosols from biomass burning, Global
696 Biogeochem. Cycles, 15(4), pp. 955–966, doi: 10.1029/2000GB001382, 2001.

697 Annegarn, H.J., van Grieken, R.E., Bibby, D.M. and von Blottnitz, F.: Background Aerosol Composition in the
698   Namib Desert, South West Africa (Namibia), Atmospheric Environment, 17(10), pp. 2045–2053, doi:
699   10.1016/0004-6981(83)90361-X, 1983.

700 Ayers, G.P., Ivey, J.P. and Goodman, H.S.: Sulfate and Methanesulfonate in the Maritime Aerosol at Cape Grim,
701   Tasmania, J. Atmos. Chem., 4, pp. 173–185, doi: 10.1007/BF00053777, 1986.

702 Baboukas, E.D., Kanakidou, M. and Mihalopoulos, N.: Carboxylic acids in gas and particulate phase above
703   the Atlantic Ocean, J. Geophys. Res., 105(D11), pp. 14459–14471, doi: 10.1029/1999JD900977, 2000.

704 Becagli, S., Anello, F., Bommarito, C., Cassola, F., Calzolai, G., Di Iorio, T., Di Sarra, A., Gómez-Amo, J.L.,
705   Lucarelli, F., Marconi, M., Meloni, D., Monteleone, F., Nava, S., Pace, G., Severi, M., Massimiliano Sferlazzo,
706   D., Traversi, R. and Udisti, R.: Constraining the ship contribution to the aerosol of the central
707   Mediterranean, Atmos. Chem. Phys., 17(3), pp. 2067–2084, doi: 10.5194/acp-17-2067-2017, 2017.

708 Boni, M. Terracciano, R., Evans, N.J., Laukamp, C., Schneider, J. and Bechstädt, T.: Genesis of Vanadium Ores
709   in the Otavi Mountainland, Namibia. Economic Geology; 102 (3), pp. 441–469, doi:
710   10.2113/gsecongeo.102.3.441, 2007.

711 Boucher, O.: Atmospheric Aerosols: Properties and climate impacts, Springer: Netherlands, 2013.

712 Calastrini, F., Del Carmine, P., Lucarelli, F., Mandò, P. A., Prati, P., and Zucchiatti, A.: External-beam PIGE for
713   fluorine determination in atmospheric aerosol, Nuclear Instruments and Methods in Physics Research
714   Section B: Beam Interactions with Materials and Atoms, 136-138, pp. 975-980, doi: 10.1016/S0168-
715   583X(97)00750-7, 1998.

716 Caponi, L., Formenti, P., Massabó, D., Di Biagio, C., Cazaunau, M., Pangui, E., Chevaillier, S., Landrot, G.,
717   Andreae, O.M., Kandler, K., Piketh, S., Saeed, T., Seibert, D., Williams, E., Balkanski, Y., Prati, P. and
718   Doussin, J.F.: Spectral- and size-resolved mass absorption efficiency of mineral dust aerosols in the
719   shortwave spectrum: A simulation chamber study, Atmos. Chem. Phys., 17(11), pp. 7175–7191,
720   doi:10.5194/acp-17-7175-2017, 2017.
721 Carslaw, D. and Ropkins, K.: Package 'openair': Tools for the Analysis of Air Pollution Data, [online]
722   Available from: http://www.openair-project.org/, https://github.com/davidcarslaw/openair, 2017.
723 Chance, R., Jickells, T.D. and Baker, A.R.: Atmospheric trace metal concentrations, solubility and deposition
724   fluxes in remote marine air over the south-east Atlantic, Mar. Chem., 177, pp. 1–12,
725   doi:10.1016/j.marchem.2015.06.028, 2015.
726 Charlson, R.J., Lovelock, J.E., Andreae, M.O. and Warren, S.G.: Oceanic phytoplankton, atmospheric sulphur,
727   cloud albedo and climate, Nature, 326, pp. 655–661, doi: 10.1038/326655a0, 1987.
728 Cole J. and Villacastin C. Sea surface temperature variability in the northern Benguela upwelling system,
729   and implications for fisheries research, International Journal of Remote Sensing, 21(8), pp. 1597-1617,
730   doi: 10.1080/014311600209922, 2000.
731 Dansie, A.P., Wiggs, G.F.S., Thomas, D.S.G. and Washington, R.: Measurements of windblown dust
732   characteristics and ocean fertilization potential: The ephemeral river valleys of Namibia, Aeolian Res.,
733   29(July), pp. 30–41, doi:10.1016/j.aeolia.2017.08.002, 2017.
734 De Graaf, M., Bellouin, N., Tilstra, L. G., Haywood, J. and Stammes, P.: Aerosol direct radiative effect of smoke
735   over clouds over the southeast Atlantic Ocean from 2006 to 2009, Geophys. Res. Lett., 41(21), pp. 7723–
736   7730, doi:10.1002/2014GL061103, 2014.
737 Denjean, C., Cassola, F., Mazzino, A., Triquet, S., Chevaillier, S., Grand, N., Bourrianne, T., Momboisse, G.,
738   Sellegri, K., Schwarzenbock, A., Freney, E., Mallet, M. and Formenti, P.: Size distribution and optical
739   properties of mineral dust aerosols transported in the western Mediterranean, Atmos. Chem. Phys.,
740   16(2), pp. 1081–1104, doi:10.5194/acp-16-1081-2016, 2016.
741 Eckardt, F., Kuring, N.: SeaWiFS identifies dust sources in the Namib Desert. Int. J. Remote Sens. 26 (19), pp.
742   4159–4167, doi: 10.1080/01431160500113112, 2005.
743 Eltayeb, M.A., Van Grieken, R.E., Maenhaut, W. and Annegarn, H.J.: Aerosol-Soil Fractionation for Namib
744   Desert Samples, Atmos. Environ., 27(5), pp. 669-678, doi: 10.1016/0021-8502(92)90577-I, 1993.
745 Ettler, V., Mihaljevič, M., Kříbek, B., Majer, V. and Šebek, O.: Tracing the spatial distribution and mobility of
746   metal/metalloid contaminants in Oxisols in the vicinity of the Nkana copper smelter, Copperbelt
747   province, Zambia, Geoderma, 164(1–2), pp. 73–84, doi:10.1016/j.geoderma.2011.05.014, 2011.
748 Feng, Y., Ogura, N., Feng, Z.W., Zhang, F.Z., and Shimizu, H.: The Concentrations and Sources of Fluoride in
749   Atmospheric Depositions in Beijing, China, Water, Air, and Soil Pollution, 145, pp. 95-107, doi:
750   10.1023/a:1023680112474, 2003.
751 Formenti, P., Piketh, S.J. and Annegarn, H.J.: Detection of non-sea salt sulphate aerosol at a remote coastal
752   site in South Africa: A PIXE study, Nucl. Instruments Methods Phys. Res. B, 150, pp. 332–338, 1999.
753 Formenti, P., Elbert, W., Maenhaut, W., Haywood, J. and Andreae, M. O.: Chemical composition of mineral
754   dust aerosol during the Saharan Dust Experiment (SHADE) airborne campaign in the Cape Verde region,
755   September 2000, J. Geophys. Res., 108(D18), p. 8576, doi: 10.1029/2002JD002648, 2003a.
756 Formenti, P., Elbert, W., Maenhaut, W., Haywood, J., Osborne, S. and Andreae, M.O.: Inorganic and
757   carbonaceous aerosols during the Southern African Regional Science Initiative (SAFARI 2000)
758   experiment : Chemical characteristics, physical properties, and emission data for smoke from African
759   biomass burning, 108(Safari 2000), pp. 1–16, doi: 10.1029/2002JD002408, 2003b.

760   Formenti, P., Schuetz, L., Balkanski, Y., Desboeufs, K., Ebert, M. and Kandler, K.: Recent progress in
761   understanding physical and chemical properties of mineral dust, Atmospheric Chemistry and Physics
762   Discussions, 10, pp. 31187 – 31251, doi: 10.5194/acpd-10-31187-2010, 2010.
763   Formenti, P., Caquineau, S., Desboeufs, K., Klaver, A., Chevaillier, S., Journet, E. and Rajot, J.L.: Mapping the
764   physico-chemical properties of mineral dust in western Africa: mineralogical composition. Atmospheric
765   Chemistry and Physics Discussions, European Geosciences Union, 2014, 14 (19), pp. 10663-10686, doi:
766   10.5194/acp-14-10663-2014, 2014.
767   Formenti, P., Piketh, S., Namwoonde, A., Klopper, D., Cazaunau, M., Feron, A., Gaimoz, C., Broccardo, S.,
768   Walton, N., Desboeufs, K., Siour, G., Burger, R., Hanghome, M., Mafwila, S., Omoregie, E., Junkermann, W.
769   and Maenhaut, W.: Three years of measurements of light-absorbing aerosols in the marine air at Henties
770   Bay, Namibia: seasonality, origin, and transport, Atmos. Chem. Phys. Discuss., (June), pp. 1–28,
771   doi:10.5194/acp-2017-471, 2018.
772   Formenti, P., D'Anna, B., Flamant, C., Mallet, M., Piketh, S.J., Schepanski, K., Waquet, F., Auriol, F., Brogniez,
773   G., Burnet, F., Chaboureau, J., Chauvigné, A., Chazette, P., Denjean, C., Desboeufs, K., Doussin, J., Elguindi,
774   N., Feuerstein, S., Gaetani, M., Giorio, C., Klopper, D., Mallet, M.D., Nabat, P., Monod, A., Solmon, F.,
775   Namwoonde, A., Chikwililwa, C., Mushi, R., Welton, E.J. and Holben, B.: The Aerosols, Radiation and
776   Clouds in southern Africa (AEROCLO-sA) field campaign in Namibia: overview, illustrative observations
777   and way forward. Bulletin of the American Meteorological Society, [online] Available at:
778   https://doi.org/10.1175/BAMS-D-17-0278.1, 2019.
779   Gillett, R., Galbally, I., Ayers, G., Selleck, P., Powell, J., Meyer, M., Keywood, M. and Fedele, R.: Oxalic acid and
780   oxalate in the atmosphere. [online] Available from: http://www.scopus.com/inward/record.url?eid=2-
781   s2.0-80053171171&partnerID=40&md5=08470ecaa392611cb869e54dddff0a16, 2007.
782   Gomez-Caminero, A., Howe, P., Hughes, M., Kenyon, E., Lewis, D., Moore, M., Ng, J., Aitio, A. and Becking, G.:
783   Arsenic and Arsenic Compounds, Geneva. [online] Available from:
784   https://apps.who.int/iris/handle/10665/42366, 2001.
785   Hedberg, E., Gidhagen, L. and Johansson, C.: Source contributions to PM10 and arsenic concentrations in
786   Central Chile using positive matrix factorization, Atmos. Environ., 39(3), pp. 549–561, doi:
787   10.1016/j.atmosenv.2004.11.001, 2005.
788   Heine, K. and Völkel, J.: Soil Clay Minerals in Namibia and Their Significance for the Terrestrial and Marine
789   Past Global Change Research, Afr. Study Monogr., 40(March), pp. 31–50, doi: 10.14989/96299, 2010.
790   Henderson, P. and Henderson, G.M.: Earth science data, Cambridge University Press, pp. 42–44, 2009.
791   Huang, S., Poulain, L., Van Pinxteren, D., Van Pinxteren, M., Wu, Z., Herrmann, H. and Wiedensohler, A.:
792   Latitudinal and Seasonal Distribution of Particulate MSA over the Atlantic using a Validated
793   Quantification Method with HR-ToF-AMS, Environ. Sci. Technol., 51(1), pp. 418–426, doi:
794   10.1021/acs.est.6b03186, 2017.
795   Isakson, J., Persson, T.A. and Lindgren, E.S.: Identification and assessment of ship emissions and their effects
796   in the harbour of Göteborg, Sweden, Atmos. Environ., 35(21), pp. 3659–3666, doi: 10.1016/S1352-
797   2310(00)00528-8, 2001.
798   Johansson, L., Jalkanen, J. and Kukkonen, J.: Global assessment of shipping emissions in 2015 on a high
799   spatial and temporal resolution, Atmos. Environ., 167, pp. 403–415, doi:
800   10.1016/j.atmosenv.2017.08.042, 2017.
801   Johnson, B.T., Shine, K.P. and Forster, P.M.: The semi-direct aerosol effect: Impact of absorbing aerosols on
802   marine stratocumulus, pp. 1407–1422, doi: 10.1256/qj.03.61, 2004.

803 Jordi, A., Basterretxea, G., Tovar-Sanchez, A., Alastuey, A. and Querol, X.: Copper aerosols inhibit
804   phytoplankton growth in the Mediterranean Sea, Proc. Natl. Acad. Sci., 109(52), pp. 21246–21249, doi:
805   10.1073/pnas.1207567110, 2012.

806 Klein, S.A. and Hartmann, D.L.: The Seasonal Cycle of Low Stratiform Clouds, J. Clim., 6, pp. 1587–1606, doi:
807   10.1175/1520-0442(1993)006<1587:TSCOLS>2.0.CO;2,1993.

808 KPMG: Namibia Country mining guide: Strategy series, [online] Available from:
809   https://assets.kpmg.com/content/dam/kpmg/pdf/2014/09/namibia-mining-guide.pdf, 2014.

810 Kříbek, B., Šípková, A., Ettler, V., Mihaljevič, M., Majer, V., Knésl, I., Mapani, B., Penížek, V., Vaněk, A. and
811   Sracek, O.: Variability of the copper isotopic composition in soil and grass affected by mining and
812   smelting in Tsumeb, Namibia, Chem. Geol., 493, pp. 121–135, doi: 10.1016/j.chemgeo.2018.05.035,
813   2018.

814 Lee, E., Chan, C.K. and Paatero, P.: Application of positive matrix factorization in source apportionment of
815   particulate pollutants in Hong Kong, 33(19), pp. 3201-3212, doi: 10.1016/S1352-2310(99)00113-2,
816   1999.

817 Lindesay, J.A., Andreae, M.O., Goldammer, J.G., Harris, G., Annegarn, H.J., Garstang, M., Scholes, R.J. and van
818   Wilgen, B.W.: International Geosphere-Biosphere Programme/International Global Atmospheric
819   Chemistry SAFARI-92 field experiment: Background and overview, J. Geophys. Res., 101(D19), pp.
820   23521–23530, doi: 10.1029/96JD01512, 1996.

821 Louw, D.C., Van Der Plas, A.K., Mohrholz, V., Wasmund, N., Junker, T. and Eggert, A. Seasonal and interannual
822   phytoplankton dynamics and forcing mechanisms in the Northern Benguela upwelling system, J. Mar.
823   Sys. Elsevier B.V., 157, pp. 124–134, doi: 10.1016/j.jmarsys.2016.01.009, 2016.

824 Morel, F.M.M. and Price, N.M.: The Biogeochemical Cycles of Trace Metals in the Oceans, Science, 300(5621),
825   pp. 944–947, doi: 10.1126/science.1083545, 2003.

826 Muhlbauer, A., McCoy, I.L. and Wood, R.: Climatology of stratocumulus cloud morphologies: Microphysical
827   properties and radiative effects, Atmos. Chem. Phys., 14(13), pp. 6695–6716, doi: 10.5194/acp-14-6695-
828   2014, 2014.

829 Namport: Annual Report, [online] Available at:
830   https://www.namport.com.na/files/documents/dee_Annual%20Report%2012%20months%20ended
831   %2031%20March%202018.pdf; last access 19 February 2020, 2018.

832 Nelson, G., and Hutchings, L.: The Benguela upwelling area. Prog. Oceanog., 12(3), 333-356, doi:
833   10.1016/0079-6611(83)90013-7, 1983.

834 Norris, G., Duvall, R., Brown, S. and Bai, S.: EPA Positive Matrix Factorization (PMF) 5.0 Fundamentals and
835   User Guide, Washington: U.S. Environmental Protection Agency, Office of Research and Development,
836   2014.

837 Okin, G.S., Baker, A.R., Tegen, I., Mahowald, N.M., Dentener, F.J., Duce, R.A., Galloway, J.N., Hunter, K.,
838   Kanakidou, M., Kubilay, N., Prospero, J.M., Sarin, M., Surapipith, V., Uematsu, M., and Zhu, T.: Impacts of
839   atmospheric nutrient deposition on marine productivity: Roles of nitrogen, phosphorus, and iron, Global
840   Biogeochemical Cycles, 25(2), pp. 1-10, doi: 10.1029/2010gb003858, 2011.

841 Paatero, P. and Tapper, U.: Positive Matrix Factorization: A non-negative factor model with optimal
842   utilization of error estimates of data values, Environmetrics, 5(2), pp. 111–126, doi:
843   10.1002/env.3170050203, 1994.

844 Paatero, P., Eberly, S., Brown, S.G. and Norris, G.A.: Methods for estimating uncertainty in factor analytic
845   solutions, 7, pp. 781–797, doi: 10.5194/amt-7-781-2014, 2014.

846 Painemal, D., Kato, S., Minnis, P., Funk, T., Hartmann, D.L., Short, D.A., Wilcox, E.M., Klein, S.A., Hartmann,
847   D.L., Review, M.W., Chand, D., Wood, R., Anderson, T.L., Satheesh, S.K., Charlson, R.J., Costantino, L., Bréon,

848   F.M., Systems, S., Systems, S., Systems, S., Darwin, E., Espy, J.P., Muhlbauer, A., McCoy, I.L., Wood, R.,
849   Medeiros, B., Zuidema, P., De Szoeke, S., Fairall, C. and Arakawa, A.: Aerosol indirect effect on warm
850   clouds over South-East Atlantic, from co-located MODIS and CALIPSO observations, Atmos. Chem. Phys.,
851   37(13), pp. 6695–6716, doi: 10.1175/1520-0469(1980)037, 2014a.

852   Painemal, D., Kato, S. and Minnis, P.: Boundary layer regulation in the southeast Atlantic cloud microphysics
853   during the biomass burning season as seen by the A-train satellite constellation, J. Geophys. Res.,
854   119(19), pp. 11288-11302, doi: 10.1002/2014JD022182, 2014b.

855   Painemal, D., Xu, K., Cheng, A., Minnis, P. and Palikonda, R.: Mean Structure and Diurnal Cycle of Southeast
856   Atlantic Boundary Layer Clouds: Insights from Satellite Observations and Multiscale Modeling
857   Framework Simulations, J. Clim., 28(1), pp. 324–341, doi: 10.1175/JCLI-D-14-00368.1, 2014c.

858   Paytan, A., Mackey, K.R.M., Chen, Y., Lima, I.D., Doney, S.C., Mahowald, N., Labiosa, R. and Post, A.F.: Toxicity
859   of atmospheric aerosols on marine phytoplankton, PNAS, 106(12), pp. 4601–4605, doi:
860   10.1073/pnas.0811486106, 2009.

861   Preston-Whyte, R.A., Diab, R.D. and Tyson, P.D.: Towards an inversion climatology of Southern Africa: Part
862   II, non-surface inversions in the lower atmosphere, South African Geogr. J., 59(1), pp. 45–59, doi:
863   10.1080/03736245.1977.9713494, 1977.

864   Prodi, F., Belosi, F., Contini, D., Santachiara, G., Di Matteo, L., Gambaro, A., Donateo, A., and Cesari, D.: Aerosol
865   fine fraction in the Venice Lagoon: Particle composition and sources, Atmospheric Research, 92(2), pp.
866   141-150, doi: 10.1016/j.atmosres.2008.09.020, 2009.

867   Quinn, P.K, Coffman, D.J., Kapustin, V.N., Bates, T.S. and Covert, D.S.: Aerosol optical properties in the marine
868   boundary layer during the First Aerosol Characterization Experiment (ACE 1) and the underlying
869   chemical and physical aerosol properties, Journal of Geophysical Research, 103(D13), pp. 16547-16563,
870   1998.

871   Sanders, J. G. and Windom, H.L.: The uptake and reduction of arsenic species by marine algae, Estuar. Coast.
872   Mar. Sci., 10(5), pp. 555–567, doi: 10.1016/S0302-3524(80)80075-2, 1980.

873   Scheifinger, H. and Held, G.: Aerosol behaviour on the South African Highveld, Atmos. Environ., 31(21), pp.
874   3497–3509, doi: 10.1016/S1352-2310(97)00217-3, 1997.

875   Seinfeld, J.H. and Pandis, S.N.: Atmospheric Chemistry and Physics: From Air Pollution to Climate Change,
876   2nd ed., John Wiley & Sons, Hoboken, New Jersey., 2006.

877   Schembari, C., Bove, M.C., Cuccia, E., Cavalli, F., Hjorth, J., Massabò, D., Nava, S., Udisti, R., and Prati, P.: Source
878   apportionment of PM10 in the Western Mediterranean based on observations from a cruise ship,
879   Atmospheric Environment, 98, pp. 510-518, doi: 10.1016/j.atmosenv.2014.09.015, 2014.

880   Šerbula, S.M., Antonijević, M.M., Milošević, N.M., Milić, S.M. and Ilić, A.A.: Concentrations of particulate
881   matter and arsenic in Bor (Serbia), J. Hazard. Mater., 181(1–3), pp. 43–51, doi:
882   10.1016/j.jhazmat.2010.04.065, 2010.

883   Shibata, Y., Sekiguchi, M., Otsuki, A. and Morita, M.: Arsenic compounds in zoo- and phyto-plankton of
884   marine origin, Appl. Organomet. Chem., 10(9), pp. 713–719, doi: 10.1002/(SICI)1099-
885   0739(199611)10:9<713::AID-AOC536>3.0.CO;2-U, 1996.

886   Sinha, P., Hobbs, P.V., Yokelson, R.J., Christian, T.J., Kirchstetter, T.W. and Bruintjes, R.: Emissions of trace
887   gases and particles from two ships in the southern Atlantic Ocean, Atmos. Environ., 37(15), pp. 2139–
888   2148, doi: 10.1016/S1352-2310(03)00080-3, 2003.

889   Soto-Viruet, Y.: The Mineral Industries of Angola and Namibia, U.S. Geol. Surv., Minerals Y(November), 1–
890   12 [online] Available from: https://www.usgs.gov/centers/nmic/africa-and-middle-east#na, 2015.

891   South   African   Weather   Service   (SAWS):   Publications.   [online]   Available   from:
892   http://www.weathersa.co.za/climate/publications. Date of access: 18 January 2017.

893   Stein, A.F., Draxler, R.R., Rolph, G.D., Stunder, B.J.B., Cohen, M.D. and Ngan, F.: Noaa's hysplit atmospheric
894   transport and dispersion modeling system, Bull. Am. Meteorol. Soc., 96(12), pp. 2059–2077, doi:
895   10.1175/BAMS-D-14-00110.1, 2015.
896   Swap, R., Garstang, M., Macko, S.A., Tyson, P.D., Maenhaut, W., Artaxo, P., Kållberg, P. and Talbot, R.: The
897   long-range transport of southern African aerosols to the tropical South Atlantic, J. Geophys. Res. Atmos.,
898   101(D19), pp. 23777–23791, doi: 10.1029/95JD01049, 1996.
899   Swap, R.J., Annegarn, H.J., Suttles, J.T., King, M.D., Platnick, S., Privette, J.L. and Scholes, R.J.: Africa burning:
900   A thematic analysis of the Southern African Regional Science Initiative (SAFARI 2000), J. Geophys. Res.
901   Atmos., 108(D13), p. 8465, doi: 10.1029/2003JD003747, 2003.
902   Theobald, M.R., Crittenden, P.D., Hunt, A.P., Tang, Y.S., Dragosits, U. and Sutton, M.A.: Ammonia emissions
903   from a Cape fur seal colony, Cape Cross, Namibia, Geophys. Res. Lett., 33(3), pp. 2–5, doi:
904   10.1029/2005GL024384, 2006.
905   Tlhalerwa, K., Freiman, M.T. and Piketh, S.J.: Aerosol Deposition off the Southern African West Coast by Berg
906   Winds, 87(2):152-161, doi: 10.1080/03736245.2005.9713838, 2012.
907   Tournadre, J.: Anthropogenic pressure on the open ocean: The growth of ship traffic revealed by altimeter
908   data analysis, Geophys. Res. Lett., 41(22), pp. 7924–7932, doi: 10.1002/2014GL061786, 2014.
909   Tyson, P.D., Garstang, M., Swap, R., Kållberg, P. and Edwards, M.: An air transport climatology for subtropical
910   Southern Africa, Int. J. Climatol., 16(3), pp. 265–291, doi: 10.1002/(SICI)1097-
911   0088(199603)16:3<265::AID-JOC8>3.0.CO;2-M, 1996.
912   Tyson, P.D. and Preston-Whyte, R.A.: The Weather and Climate of Southern Africa, 2nd ed. Oxford University
913   Press Southern Africa, Cape Town, 2014.
914   Viana, M., Amato, F., Alastuey, A., Querol, X., Moreno, T., Dos Santos, S.G., Herce, M.D. and Fernández-Patier,
915   R.: Chemical tracers of particulate emissions from commercial shipping, Environ. Sci. Technol., 43(19),
916   pp. 7472–7477, doi: 10.1021/es901558t, 2009.
917   Vickery, K.J., Eckardt, F.D., Bryant, R.G.: A sub-basin scale dust plume source frequency inventory for
918   southern Africa, 2005–2008. Geophys. Res. Lett. 40 (19), pp. 5274–5279, doi: 10.1002/grl.50968, 2013.
919   Vouk, V.B. and Piver, W.T.: Metallic Elements in Fossil Fuel Combustion Products: Amounts and Form of
920   Emissions and Evaluation of Carcinogenicity and Mutagenicity, Environ. Health Perspect., 47, pp. 201–
921   225, doi: 10.1289/ehp.8347201, 1983.
922   Wanke, H., Nakwafila, A., Hamutoko, J.T., Lohe, C., Neumbo, F., Petrus, I., David, A., Beukes, H., Masule, N. and
923   Quinger, M.: Hand dug wells in Namibia: An underestimated water source or a threat to human health?,
924   J. Phys. Chem. Earth, pp. 1–10, doi: 10.1016/j.pce.2015.01.004, 2015.
925   Wilcox, E.M.: Stratocumulus cloud thickening beneath layers of absorbing smoke aerosol, Atmos. Chem.
926   Phys., 10(23), pp. 11769–11777, doi: 10.5194/acp-10-11769-2010, 2010.
927   Wood, R.: Stratus and stratocumulus, in Encyclopedia of Atmospheric Sciences, 2nd ed., vol. 2, edited by G.
928   R. North, J. Pyle, and F. Zhang, Elsevier, pp. 196– 200, 2015.
929   Zhang, M., Chen, J.M., Wang, T., Cheng, T.T., Lin, L., Bhatia, R.S. and Hanvey, M.: Chemical characterization of
930   aerosols over the Atlantic Ocean and the Pacific Ocean during two cruises in 2007 and 2008, J. Geophys.
931   Res. Atmos., 115(22), pp. 1-15, doi: 10.1029/2010JD014246, 2010.
932   Zorn, S.R., Drewnick, F., Schott, M., Hoffmann, T. and Borrmann, S.: Characterization of the South Atlantic
933   marine boundary layer aerosol using an aerodyne aerosol mass spectrometer, Atmos. Chem. Phys., 8,
934   4711–4728 [online] Available from: www.atmos-chem-phys.net/8/4711/2008, 2008.
935   Zuidema, P., Painemal, D., De Szoeke, S. and Fairall, C.: Stratocumulus cloud-top height estimates and their
936   climatic implications, J. Clim., 22(17), pp. 4652–4666, doi: 10.1175/2009JCLI2708.1, 2009.

937   Zuidema, P., Redemann, J., Haywood, J., Wood, R., Piketh, S., Hipondoka, M. and Formenti, P.: Smoke and
938   Clouds above the Southeast Atlantic: Upcoming Field Campaigns Probe Absorbing Aerosol's Impact
939   on Climate, Bull. Am. Meteorol. Soc., 97, pp. 1131-1135, doi: 10.1175/BAMS-D-15-00082.1, 2016.

940 **Table captions**

941 **Table 1**. Summary statistics of elemental and water-soluble ionic concentrations measured at HBAO. The

942 second column indicates the number of samples for which values were above the minimum quantification

943 limit (MQL). The arithmetic means with standard deviations (sd) and range of mass concentrations

944 (minimum and maximum) are given in ng m^{-3}.

945 **Table 2**. Annual mean mass ratios of Cl$^-$, Mg^{2+}, K$^+$, Ca^{2+}, F$^-$ and SO$_4{}^{2-}$ with respect to Na$^+$ for 2016 and 2017

946 as well as the R^2 for each linear model and mass ratios for seawater reported in the literature (Seinfeld and

947 Pandis; 2006). Standard deviations are indicated as *sd*.

948 **Table 3.** Average mass ratios and standard deviations for 2016 and 2017 for dust episodes. Mass ratios

949 reported in the literature are given in the last row for comparison.

950 **Table 4.** Reported concentrations for marine biogenic and secondary aerosols for different locations, and

951 especially in the southern hemisphere. Concentrations are in μg m^{-3} unless stated otherwise.

952 **Figure captions**

953 **Figure 1.** Geographical map of Namibia with elevation as a shaded gradient and some of the known

954 emission sources in the region, such as major urban settlements and airports, harbours, pans and swamps,

955 mineral-rich mining operations, labelled by the major element begin mined, and dune fields of the Kalahari

956 stratigraphic group (Atlas of Namibia project, 2002).

957 **Figure 2.** Composite maps of 72-hour back-trajectories for every filter sampling period in 2016 (dates in

958 blue) and 2017 (dates in orange). From these composite maps, a clear distinction can be made between

959 marine air masses and those of continental origin and the potential for variability from these regions in

960 terms of distance travelled and trajectory pathway. The colours are only used to differentiate one set of

961 trajectories from another.

962 **Figure 3.** Wind roses showing the wind speed, direction and frequency of occurrence corresponding to

963 each aerosol sampling week in 2016 (dates in blue), and 2017 (dates in orange). The arithmetic mean wind

964 speed for each week is reported in green. For 7–14 July 2017 no surface wind data is available.

965 **Figure 4.** Hourly wind roses during the aerosol sampling at HBAO. The arithmetic means and percentage

966 of calm conditions, when wind speeds are below detection, is reported in green. Time is in UTC. For 7–14

967 July 2017 no surface wind data is available.

968   **Figure 5.** Time series (datetime in UTC) of measured concentrations for Na^+, Ca^{2+}, Al, K^+, SO_4^{2-}, MSA and Ni
969   (shaded area). The solid black line indicates the calculated 10-point moving average. The sea salt (ss)
970   components for Ca^{2+}, K^+ and SO_4^{2-} is indicated by the orange shaded areas, the non-sea salt (nss) fraction is
971   represented by the blue shaded areas. The time series is non-consecutive and is divided into the 26
972   sampling weeks by the light grey vertical lines.

973   **Figure 6.** Scatterplots of nss-Ca^{2+}/Al (top left), nss-K^+/Al (top right), V (bottom left) and Ni (bottom right)
974   ratios to Al for 2016 (blue) and 2017 (orange). Concentrations are expressed in $\mu g\ m^{-3}$. Note the logarithmic
975   y-axes on the top plots.

976   **Figure 7.** Scatterplots for ratios of MSA (left) and NH4+ (right) to nss-SO42- for 2016 (blue) and 2017
977   (orange). Concentrations are expressed in µg m-3. Note the logarithmic y-axis of the figure on the right.

978   **Figure 8.** Profiles of the five sources identified by the PMF analysis. Blue bars denote the mass
979   concentrations of individual elements/ionic species (left logarithmic axis, $ng\ m^{-3}$) while the yellow points
980   indicate the percent of species attributed to the source (right axis).

981

Atmospheric
Chemistry
and Physics
Discussions

982 **Table 1.** Summary statistics of elemental and water-soluble ionic concentrations measured at HBAO. The second
983 column indicates the number of samples for which values were above the minimum quantification limit (MQL). The
984 arithmetic means with standard deviations (sd) and range of mass concentrations (minimum and maximum) are given
985 in ng m^{-3}.

Chemical species	Number of samples	Mean ± sd	Range
Cl	385	13216 ± 7987	17 - 50041
S	383	1346 ± 645	1 - 4386
Ca	366	885 ± 768	75 - 6862
Fe	383	367 ± 458	3 - 3687
Na	380	8435 ± 5752	18 - 42688
Mg	380	1178 ± 792	1 - 6416
Al	379	478 ± 581	2 - 4739
Si	374	1687 ± 2102	5 - 17016
P	352	10 ± 8	1 - 72
K	379	511 ± 359	8 - 3076
Ti	367	39 ± 47	1 - 363
Mn	295	13 ± 11	1 - 86
Zn	182	12 ± 7	1 - 42
Cr	228	8 ± 6	1 - 31
V	334	8 ± 5	1 - 38
Ba	100	9 ± 7	1 - 34
Co	261	8 ± 5	1 - 32
Cu	228	13 ± 9	1 - 48
Nd	296	15 ± 11	1 - 61
Ni	278	8 ± 6	1 - 33
Sr	251	77 ± 63	2 - 346
Cd	214	735 ± 1124	1 - 6776
As	221	191 ± 317	1 - 1092
Pb	193	75 ± 89	1 - 509
F$^-$	375	3356 ± 3201	110 - 25240
Acetate	90	27 ± 36	11 - 235
Propionate	79	46 ± 21	12 - 162
Formate	322	23 ± 12	5 - 73
MSA	330	63 ± 38	11 - 232
Cl$^-$	376	13980 ± 9834	117 - 76008
Br$^-$	17	44 ± 15	27 - 77
NO$_3^-$	364	232 ± 432	26 - 8167
PO$_4^-$	41	60 ± 62	27 - 397
SO$_4^{2-}$	376	3602 ± 1853	81 - 14331
Oxalate	379	121 ± 53	13 - 474
Na$^+$	376	10199 ± 6853	32 - 52987
NH$_4^+$	376	205 ± 126	25 - 1747
K$^+$	373	413 ± 265	23 - 1976
Mn^{2+}	7	41 ± 35	22 - 117
Ca^{2+}	371	727 ± 618	35 - 5232
Mg^{2+}	370	1168 ± 768	29 - 5585

986

987 **Table 2.** Annual mean mass ratios of Cl^-, Mg^{2+}, K^+, Ca^{2+}, F^- and SO_4^{2-} with respect to Na^+ for 2016 and 2017 as well as
988 the R^2 for each linear model and mass ratios for seawater reported in the literature (Seinfeld and Pandis; 2006).
989 Standard deviations are indicated as *sd*.

	2016		2017		Average seawater
	Mass ratio ± sd	R^2	Mass ratio ± sd	R^2	Mass ratio
Cl^-/Na^+	1.35 ± 0.11	0.99	1.34 ± 0.11	0.99	1.80
Mg^{2+}/Na^+	0.12 ± 0.01	0.99	0.11 ± 0.01	0.99	0.12
K^+/Na^+	0.04 ± 0.01	0.98	0.04 ± 0.01	0.93	0.04
Ca^{2+}/Na^+	0.07 ± 0.04	0.61	0.07 ± 0.05	0.42	0.04
SO_4^{2-}/Na^+	0.36 ± 0.14	0.95	0.42 ± 0.23	0.85	0.25
F^-/Na^+	0.38 ± 0.24	0.53	0.32 ± 0.35	0.33	0.000122

990

991

Atmospheric
Chemistry
and Physics
Discussions

992

Table 3. Average mass ratios and standard deviations for 2016 and 2017 for dust episodes. Mass ratios reported in the literature are given in the last row for comparison.

	2016		2017		Dust episodes		Literature values
	Mean (± sd)	R^2	Mean (± sd)	R^2	Mean (± sd)	R^2	
Si/Al	3.75 ± 1.04	0.96	3.51 ± 0.74	0.96	3.60 ± 0.65	0.94	2.87 – 6.13[a], 3.41[b], 4.63[c]
nss-Ca^{2+}/Al	1.27 ± 0.67	0.89	0.5 ± 0.37	0.83	1.42 ± 0.87	0.60	0.35 – 6.06[a], 0.19[c]
Fe/Al	0.75 ± 0.19	0.96	0.81 ± 0.20	0.97	0.81 ± 0.11	0.97	0.65 – 1.06[b], 0.53[c]
V/Al	0.03 ± 0.03	0.37	0.03 ± 0.04	0.26	0.02 ± 0.03	0.31	0.0014[c]
Ti/Al	0.07 ± 0.22	0.96	0.1 ± 0.04	0.97	0.08 ± 0.02	0.97	0.09 – 0.15[a], 0.07[c]
P/Al	0.03 ± 0.02	0.81	0.03 ± 0.03	0.59	0.02 ± 0.01	0.72	0.007[d]
Fe/nss-Ca^2	0.66 ± 0.23	0.94	2.73 ± 25.81	0.83	8.57 ± 77.71	0.60	0.18 – 1.86[a], 0.58[b], 2.77[c]
nss-K$^+$/Al	0.13 ± 0.12	0.81	0.13 ± 0.13	0.59	0.08 ± 0.06	0.61	0.251 – 0.452[a]
V/Si	0.01 ± 0.01	0.39	0.01 ± 0.01	0.26	0.01 ± 0.01	0.33	0.0003[c]
F$^-$/Al	11.75 ± 8.40	0.73	9.66 ± 8.38	0.64	6.90 ± 4.56	0.57	–
nss-SO$_4^{2-}$/nss-Ca^{2+}	5.32 ± 6.79	0.08	8.72 ± 44.24	0.03	3.21 ± 5.73	0.11	2.4 [e]

995
996 [a] Eltayeb et al., (1993) from various sites around the Central Namib
997 [b] Annegarn et al. (1983): Gobabeb, Namibia
998 [c] Seinfeld and Pandis (2006): average chemical composition for soils globally
999 [d] Formenti et al., (2003): Cape Verde region
1000 [e] Molar mass ratio for gypsum
1001

34

Atmospheric
Chemistry
and Physics

Discussions

Open Access

Table 4. Reported concentrations for marine biogenic and secondary aerosols for different locations, and especially in the southern hemisphere. Concentrations are in µg m^{-3} unless stated otherwise.

	SO$_4^{2-}$ (nss-SO$_4^{2-}$)	NH$_4^+$	NO$_3^-$	MSA	MSA/nss-SO$_4^{2-}$
Outflow Africa south of Cape Town, PM1 [a]	1.39	0.18	0.01	0.04	0.007 [aaa]
Southern Ocean south of Australia [b]	-	-	-	0.02 - 0.2	0.24 ± 0.16
Cape Grim, Tasmania [c]	11.9 ± 1.2 nmole/m^3	-	-	0.167 ± 0.027 nmole/m^3	0.063 ± 0.020
19°S offshore southern Africa [d]	-	-	-	6.1 ± 4 ppt; 6.3 ± 4.4 ppt	0.05 - 0.11
Southern Atlantic [e] **A = autumn, S = spring** [f]	1.95 ± 1.05 [e]	7.6 ± 13.9 [e]	1.05 ± 0.72 [e]	0.21 ± 0.30 [e] S: 0.05 ± 0.1 [j] A: 0.15 ± 0.1 [j]	0.11 [e]
Southern Pacific [e]	2.10 ± 1.05	0 ± 0	0.12 ± 0.15	0.58 ± 0.60	0.27
Venice Lagoon [g] **W = winter, S = spring**	W: 3.3 ± 1.0; S: 4.4 ± 1.2	W: 2.9 ± 0.6 S: 2.6 ± 1.0	W: 9.0 ± 2.4 S: 3.5 ± 2.9	W: 0.035 ± 0.017 S: 0.054 ± 0.040	0.1
Southern Indian Ocean [h]	-	-	-	-	0.1
America Samoa (14°S, 170°W) [i]	-	-	-	-	0.06
Coastal Antarctica [j]	-	-	-	-	0.05 - 0.17
This study; 2016	4.0 ± 2.4 (1.7 ± 0.8)	0.19 ± 0.10	0.26 ± 0.71	0.07 ± 0.01	0.03 ± 0.01
This study; 2017	3.4 ± 1.4 (1.6 ± 0.7)	0.20 ± 0.10	0.22 ± 0.12	0.07 ± 0.04	0.04 ± 0.02

[a] Zorn et al. (2008); PM1 fraction, [aaa] calculated with respect to total sulphate
[b] Quinn et al. (1998)
[c] Ayers et al. (1986)
[d] Andreae et al. (1995)
[e] Zhang et al. (2010); total suspended particulates fraction
[f] Huang et al. (2016)
[g] Prodi et al. (2009)
[h] Sciare et al. (2000)
[i] Savoie et al. (1994)
[j] Chen et al. (2012)

Atmospheric
Chemistry
and Physics
Discussions

Figure 1. *Geographical map of Namibia with elevation as a shaded gradient and some of the known emission sources in the region, such as major urban settlements and airports, harbours, pans and swamps, mineral-rich mining operations, labelled by the major element begin mined, and dune fields of the Kalahari stratigraphic group (Atlas of Namibia project, 2002).*

Atmospheric
Chemistry
and Physics

Discussions

Open Access

EGU

1024 **Figure 2.** *Composite maps of 72-hour back-trajectories for every filter sampling period in 2016 (dates in blue) and 2017*
1025 *(dates in orange). From these composite maps, a clear distinction can be made between marine air masses and those of*
1026 *continental origin and the potential for variability from these regions in terms of distance travelled and trajectory*
1027 *pathway. The colours are only used to differentiate one set of trajectories from another.*
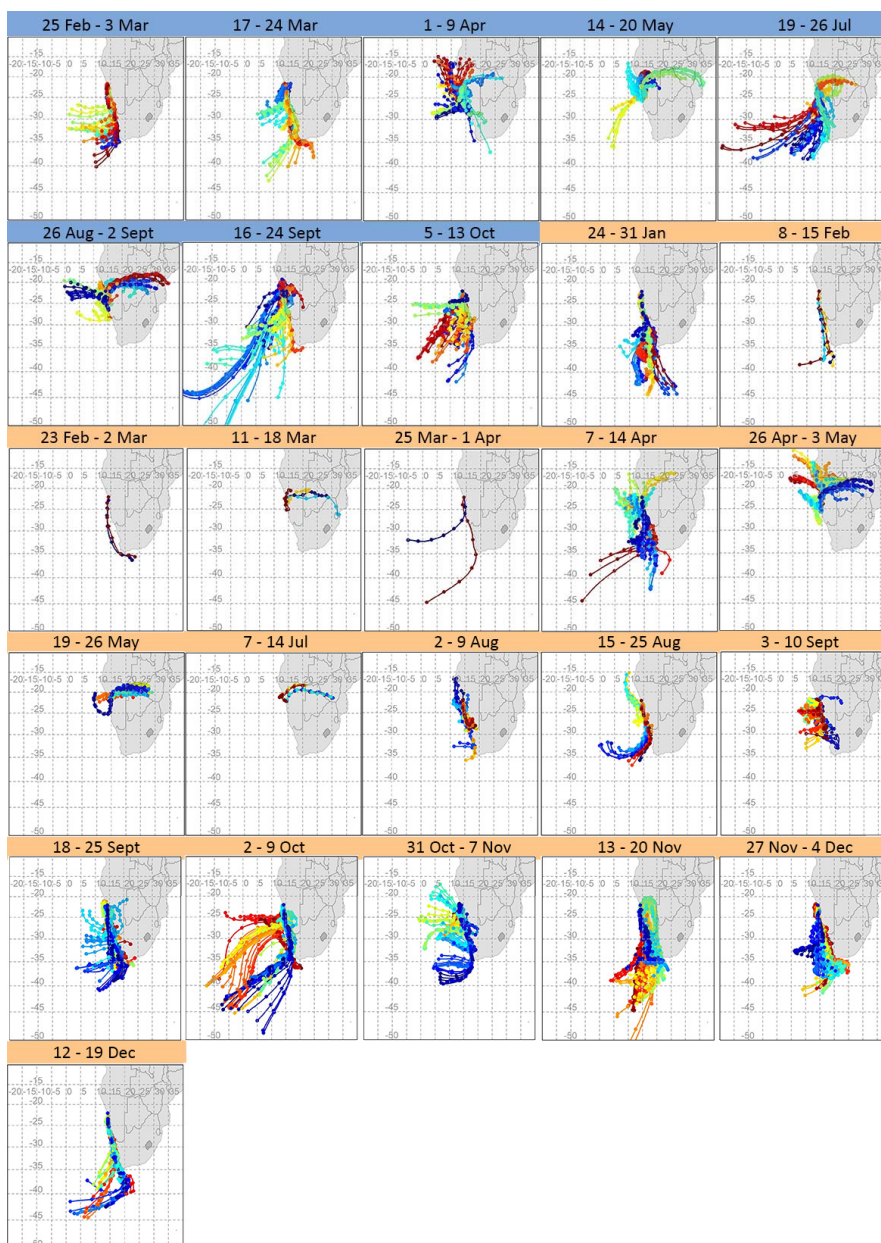
1028

Figure 3. *Wind roses showing the wind speed, direction and frequency of occurrence corresponding to each aerosol sampling week in 2016 (dates in blue), and 2017 (dates in orange). The arithmetic mean wind speed for each week is reported in green. For 7–14 July 2017 no surface wind data is available.*
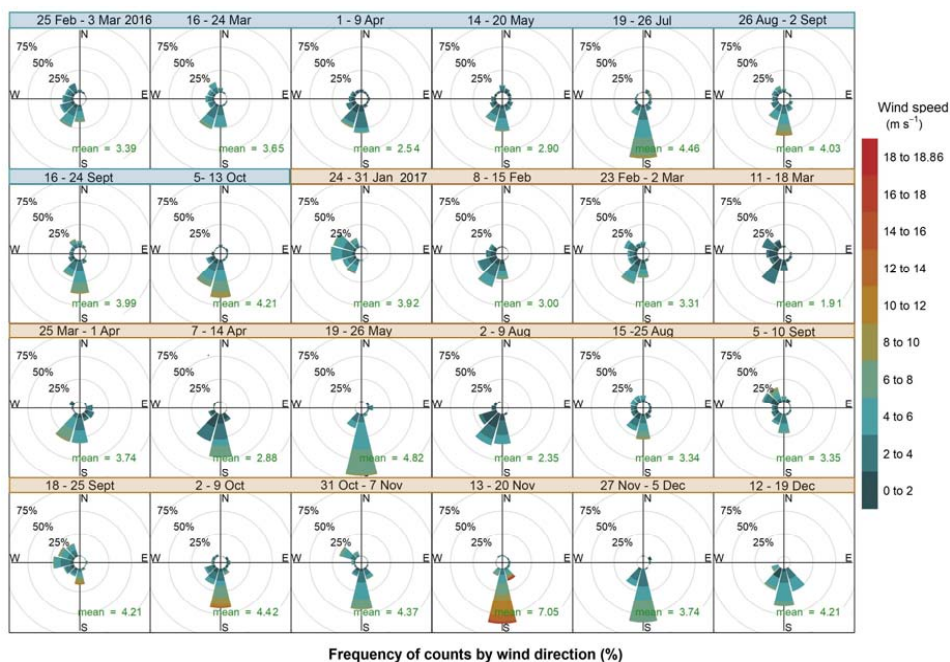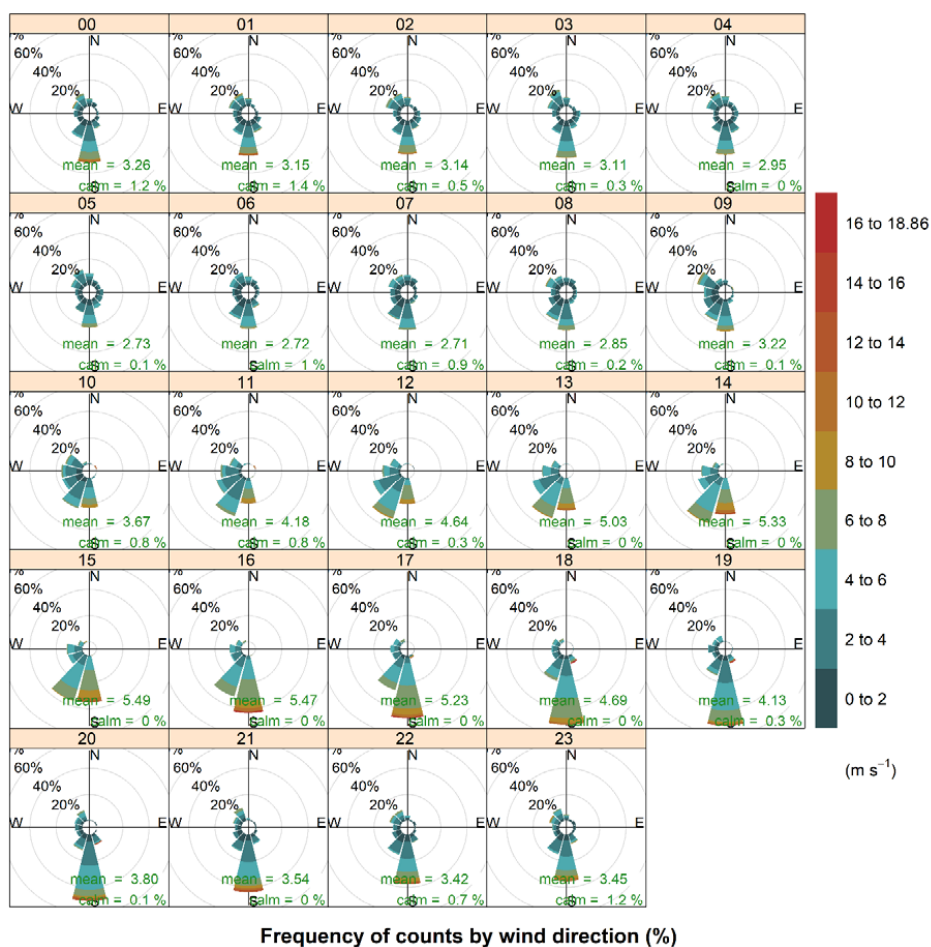
1034   **Figure 4.** *Hourly wind roses during the aerosol sampling at HBAO. The arithmetic means and percentage of calm*
1035   *conditions, when wind speeds are below detection, is reported in green. Time is in UTC. For 7–14 July 2017 no surface*
1036   *wind data is available.*

1037

1038

1039 **Figure 5.** *Time series (datetime in UTC) of measured concentrations for Na⁺, Ca²⁺, Al, K⁺, SO₄²⁻, MSA and Ni (shaded area).*
1040 *The solid black line indicates the calculated 10-point moving average. The sea salt (ss) components for Ca²⁺, K⁺ and SO₄²⁻*
1041 *is indicated by the orange shaded areas, the non-sea salt (nss) fraction is represented by the blue shaded areas. The time*
1042 *series is non-consecutive and is divided into the 26 sampling weeks by the light grey vertical lines.*

1043

1044

Atmospheric
Chemistry
and Physics
Discussions

Open Access

EGU
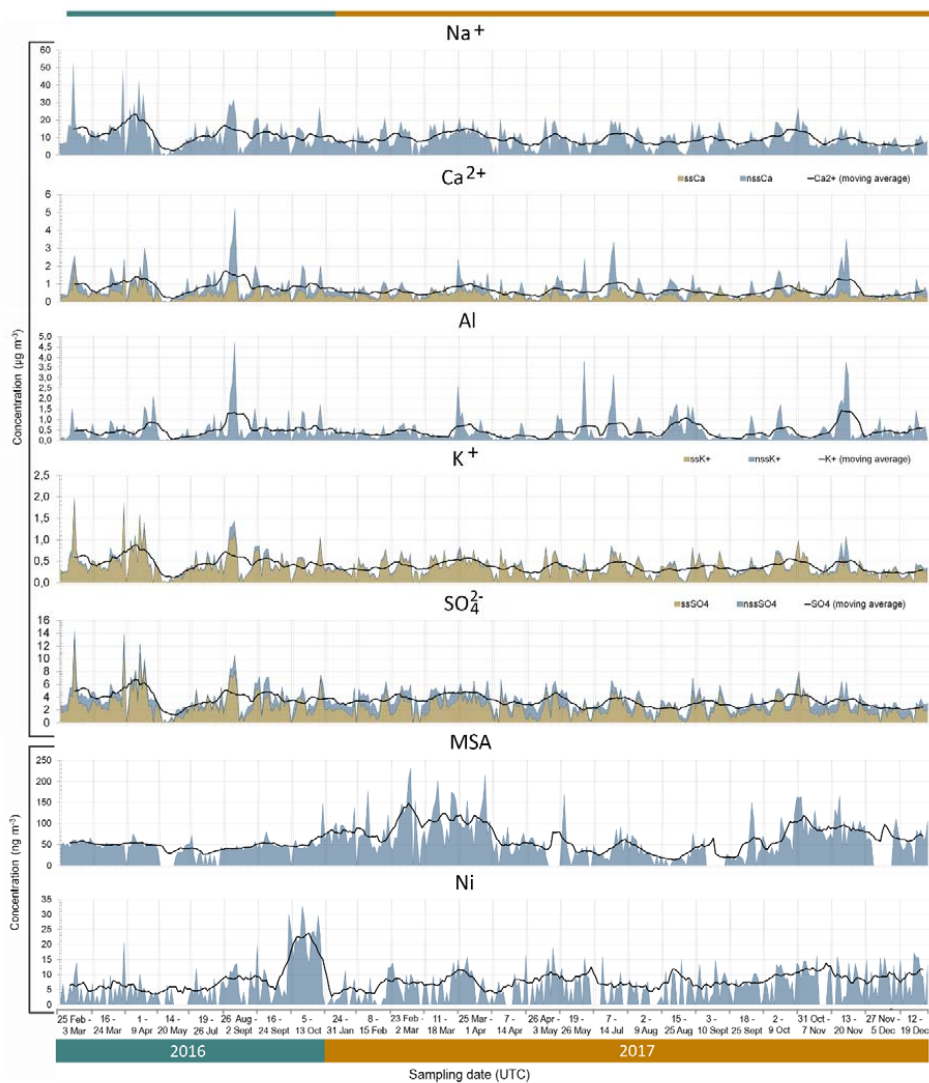
1045   ***Figure 6.*** *Scatterplots of nss-Ca²⁺/Al (top left), nss-K⁺/Al (top right), V (bottom left) and Ni (bottom right) ratios to Al for*
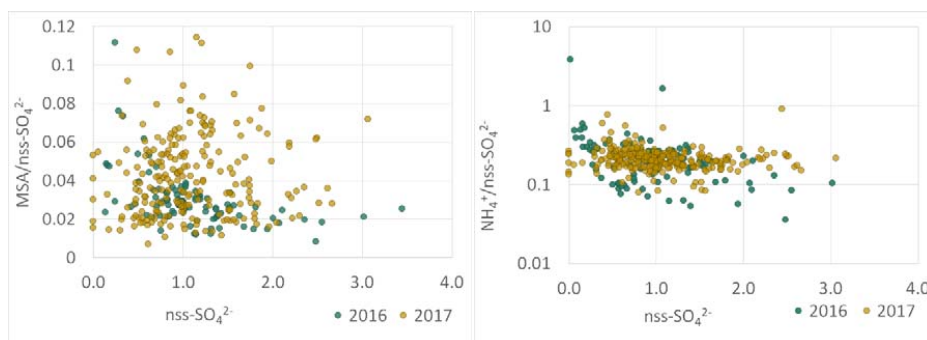1046   *2016 (blue) and 2017 (orange). Concentrations are expressed in µg m⁻³. Note the logarithmic y-axes on the top plots.*
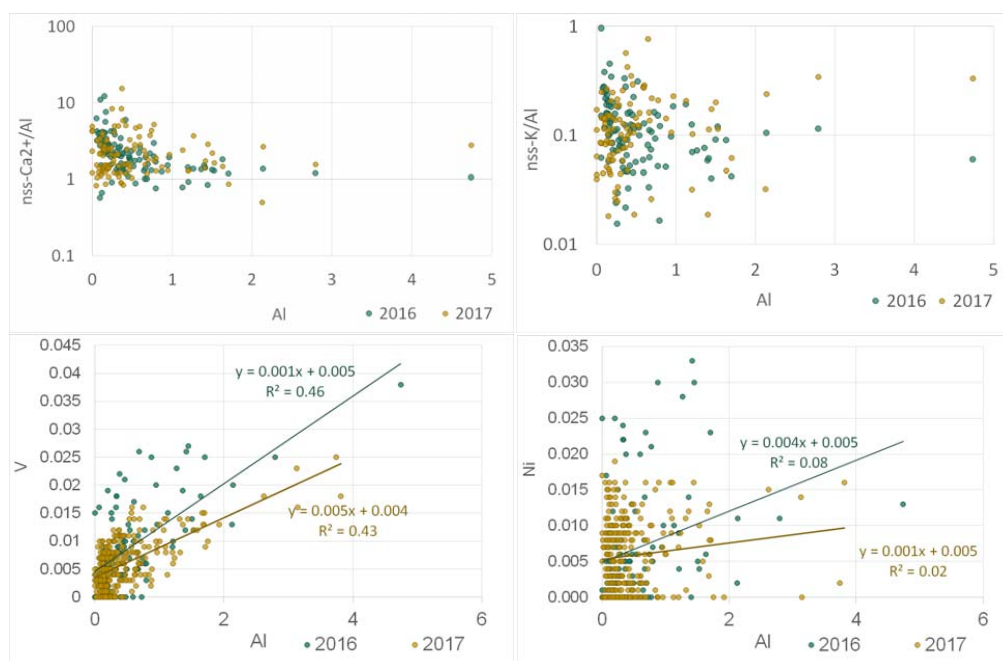
1047

1048

1049

1050   **Figure 7.** *Scatterplots for ratios of MSA (left) and NH4+ (right) to nss-SO42- for 2016 (blue) and 2017 (orange).*
1051   *Concentrations are expressed in μg m-3. Note the logarithmic y-axis of the figure on the right.*

1055 **Figure 8.** *Profiles of the five sources identified by the PMF analysis. Blue bars denote the mass concentrations of individual*
1056 *elements/ionic species (left logarithmic axis, ng m⁻³) while the yellow points indicate the percent of species attributed to*
1057 *the source (right axis).*

1058